

UNIVERSITY OF TARTU  
Faculty of Science and Technology  
Institute of Technology

Kristian Kuppert

**NANOCRYSTALLINE COPPER SIMULATIONS IN HIGH ELECTRIC  
FIELDS**

Bachelor's thesis

Supervisor: Vahur Zadin

Co-supervisor: Flyura Djurabekova

Tartu 2015

# Contents

<b>Introduction</b>	<b>3</b>
<b>1 Background</b>	<b>6</b>
1.1 Electrical breakdowns in vacuum . . . . .	6
1.2 Crystal structures of metals . . . . .	6
1.3 Defects in metals . . . . .	8
1.3.1 Dislocations . . . . .	9
1.3.2 Stacking faults . . . . .	9
1.3.3 Grain boundaries . . . . .	9
<b>2 Methodology</b>	<b>11</b>
2.1 Classical molecular dynamics(MD) . . . . .	11
2.1.1 Numerical integration schemes for MD simulations . . . . .	12
2.1.2 Embedded atom method(EAM) and EAM potentials . . . . .	13
2.1.3 Atomic stress calculations . . . . .	14
2.1.4 Potential cut-off value . . . . .	15
2.1.5 Periodic boundary conditions . . . . .	15
2.1.6 Equilibration . . . . .	15
2.1.7 Simulated annealing . . . . .	16
2.2 Analysis methods of crystalline structures . . . . .	17
2.2.1 Centrosymmetry parameter(CSP) . . . . .	17
2.2.2 Common Neighbour Analysis(CNA) . . . . .	17
2.2.3 Coordination Analysis . . . . .	18
2.3 Used software . . . . .	18
2.4 The electric field distribution at the material surface . . . . .	19
2.4.1 Detection of the surface atoms . . . . .	19
2.4.2 Creating a smooth surface for electric field calculations . . . . .	20
2.4.3 Calculating the electric field . . . . .	21
2.4.4 The effect of electrostatic forces on the surface atoms . . . . .	21
<b>3 Simulations</b>	<b>23</b>
3.1 Test case for the surface construction and electric field distribution . . . . .	23
3.2 Preparing the sample . . . . .	23
3.2.1 Setup and initial geometry . . . . .	23
3.2.2 Energy minimization . . . . .	24
3.2.3 Temperature ramping . . . . .	25
3.2.4 Equilibration . . . . .	25
3.2.5 Simulated annealing . . . . .	25

3.3	Applying the electric field . . . . .	26
3.3.1	Constant electric field . . . . .	26
3.3.2	Spatially varying electric field . . . . .	27
<b>4</b>	<b>Results and analysis</b>	<b>28</b>
4.1	Surface reconstruction and electric field calculation for the test geometry . . . . .	28
4.2	Surface reconstruction from molecular dynamics data for the system . . . . .	29
4.3	The electric field calculation with Finite Element Method . . . . .	30
4.4	Results of preparing the sample . . . . .	31
4.5	MD Simulation results of material under constant surface electric field . . . . .	33
4.6	MD simulation results of material under spatially varying surface electric field .	34
4.7	Discussion . . . . .	36
	<b>Summary</b>	<b>37</b>
	<b>Kokkuvõte</b>	<b>37</b>
	<b>Bibliography</b>	<b>40</b>

# Introduction

## Compact Linear Collider(CLIC)

With the rise of available computational power, computational material science has emerged as a field which is both promising [1] and challenging, allowing us to simulate conditions, which would be experimentally hard to attain and to understand the microscopic phenomena that govern the macroscopic behaviour of materials [2]. In particular, atomistic modelling techniques have been used to study vacuum breakdowns caused by material failure in fusion reactors [3] and particle accelerators [4]. In Compact Linear Collider CLIC [5], a new planned electron-positron collider at CERN, planned energies of the electron-positron beam will peak at 5 TeV, with optimal working energy of 3 TeV [5]. To achieve those energies, huge accelerating radio frequency electric fields over 100 MV/m are needed. The magnitude of the accelerating field and thereby the achievable energy is mainly limited by electrical breakdowns in ultra-high vacuum conditions in the accelerating structures [6, 4]. These breakdowns can damage the material [7] and cause the loss of the accelerated beam [8]. The driving mechanisms behind these breakdowns are not known, it has been speculated, that they are caused by evaporation of atoms from the surface [9], electron emission [8] or other mechanisms, that lead to plasma formation near the metal surface [9]. As most of these processes need much higher electric fields than the observed critical electric field value to be activated, the explanation for this kind of electrical breakdown in vacuum remains insufficient. Nevertheless, it has been experimentally shown, that in some regions on the surface, the local field is stronger than the applied macroscopic field by a factor of  $\beta = 50 - 100$  [7], which can cause evaporation of surface atoms and electron emission from those regions. There are many possible explanations for this kind of field enhancement. One of the most studied explanation is that this microscopic field enhancement originates from narrow protrusions on the metal surface [6], which are preferred on-sites for evaporation due to higher electric fields and electron emission due to heating from conduction currents. The mechanisms for the origin or development of those field emitters are not well understood, because such protrusions should be well seen under an electron microscope and no geometrical protrusion with  $\beta > 50$  has been experimentally found [7]. It has been proposed, that these kinds of field emitters might dynamically grow on the electrode surface due to tensile stress exerted by the electric field on the material surface, as it has been verified, that the probability of a breakdown depends on the structural properties of the materials used [8]. Different underlying causes by structural defects beneath the metal surface for the growth of these protrusion have been proposed, for example it has been shown by simulations[10, 11], that a pre-existing void underneath the copper surface in a strong external electric field can cause significant surface modification, which in-turn causes enhancement of the local electric field, leading to a self-reinforcing process[10]. Also it has been shown that a pre-existing iron precipitate under the copper surface can cause dislocation emission from the interface between

the copper lattice and the precipitate[12], causing structural modification of the surface. As the surface modification under applied electric fields could be caused by a number of defects not yet studied, further work has to be conducted to study the effects of those defects. The present work focuses on molecular dynamics simulations of defects found in nano-crystalline copper and the possible surface modification caused by those defects. The aim of this work is the following:

- Prepare a computer model of nano-crystalline copper and prepare it for further simulations
- Analyze the structure and defects of the resulting sample
- Develop methodology to couple molecular dynamics simulations with continuum calculations of the electric field to take into account pre-existing surface roughness
- Use the developed methods to study the surface morphology and failure mechanisms of the prepared sample

This thesis is split into 4 chapters. The first chapter discusses the origins of electrical breakdowns in vacuum and gives an overview of crystal structures of metals and types of defects found in those structures. Overview of molecular dynamics, used algorithms, methods and software is discussed in chapter 2. Description and setups of ran simulations is discussed in chapter 3 and results with analysis is presented in chapter 4.

# 1 Background

## 1.1 Electrical breakdowns in vacuum

Electrical breakdown is a process where a sudden reduction in the resistance of an insulator occurs when the electric field in the insulator reaches some critical value  $E_{cr}$  [13]. This phenomenon is most easily explained in the case of dielectric breakdown in gases, of which lightning is a prime example. If the voltage between the electrodes separated by the gas increases so that the electric field in the gas exceeds the dielectric strength of the gas, the electric field ionizes the gas and it becomes conductive, which allows for an electric discharge in the form of a spark to develop between the electrodes. In the case of vacuum, there is no matter between the electrodes and this kind of dielectric breakdown cannot occur. For that reason, vacuum has been used extensively in high voltage devices like X-ray tubes, electron microscopes, particle accelerators, etc [13]. Even though in the case of vacuum insulation the breakdown voltage is increased, unpredictable electrical breakdown in the form of arcing can still occur between the electrodes. In the case of partial vacuum, this arcing can be attributed to residual gas between the electrodes, but in the case of ultra-high vacuum it can only be caused by the increase of the partial pressure of the electrode material in the gap [13] [14]. For that reason, any physical explanation given for the breakdown in ultra high vacuum conditions must describe the surface processes on the electrode surface, which lead to vaporization of the electrode material. Early studies of vacuum breakdown mechanisms show that before a breakdown event, the vacuum gap has a small but finite conductivity, which increases rapidly as the electric field approaches the breakdown field. The current originates from a field emission process on small spots on the cathode surface [13], which indicates a local field enhancement in those spots.

## 1.2 Crystal structures of metals

The internal structure of metals and many other types of solids is crystalline, meaning that the atoms inside the solid are arranged in a periodic pattern that repeats itself infinitely [15]. The arrangement of the atoms in a crystal is called its crystal structure. The crystal structure can be described by a lattice that consists of three sets of parallel infinite lines. Those lines create a repeating pattern of parallelepipeds which is called the unit cell of the lattice. By placing atoms in the unit cell and repeating the resulting pattern infinitely in every direction, the crystal structure is obtained. The unit cell is defined by its dimensions  $a, b, c$  and its internal angles  $\alpha, \beta, \gamma$  (see Figure 1.2.1). It can be shown, that there exist 14 distinct types of lattices in three dimension which differ by their parameters of the position of the lattice points in the unit cell.

For metals, the most common crystal structures are face-centered cubic structure (fcc), body-centered cubic structure (bcc) and hexagonal close-packed structure (hcp). In the fcc structure, the lattice parameters  $a, b, c$  are all equal and simply called the lattice parameter. The angles are  $\alpha, \beta, \gamma = 90^\circ$ . The atoms are situated at the corners of the unit cell and at the centers of the cube faces (see Figure 1.2.2). The stacking sequence of atoms in the closest packed direction is ABCABC, meaning that the pattern of atoms in that direction repeats after 3 atomic layers. The smallest distance between atomic sites is  $\frac{\sqrt{2}}{2}a$ , where  $a$  is the lattice parameter. Notable metals with a fcc structure include copper, aluminum, gold and silver. In body-centered cubic structure the atoms are located at the corners of the unit cell and 1 atom is in the middle of the unit cell (see Figure 1.2.3a). The smallest distance between atomic sites is  $\frac{\sqrt{3}}{4}a$ . Notable metals with bcc structure include iron, chromium and tungsten. In hcp structure the unit cell is more complex but it can be easily visualized as two interleaving hexagonal atomic layers repeating infinitely. The stacking sequence in this configuration is ABAB. Metals with hcp structure include zinc, magnesium and Cadmium.

Figure 1.2.1: Unit cell of a crystal [15]

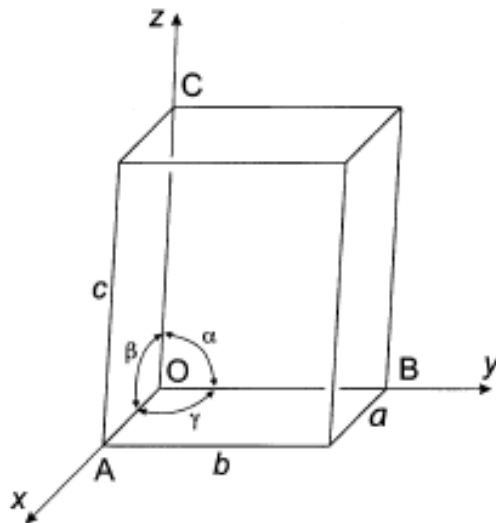
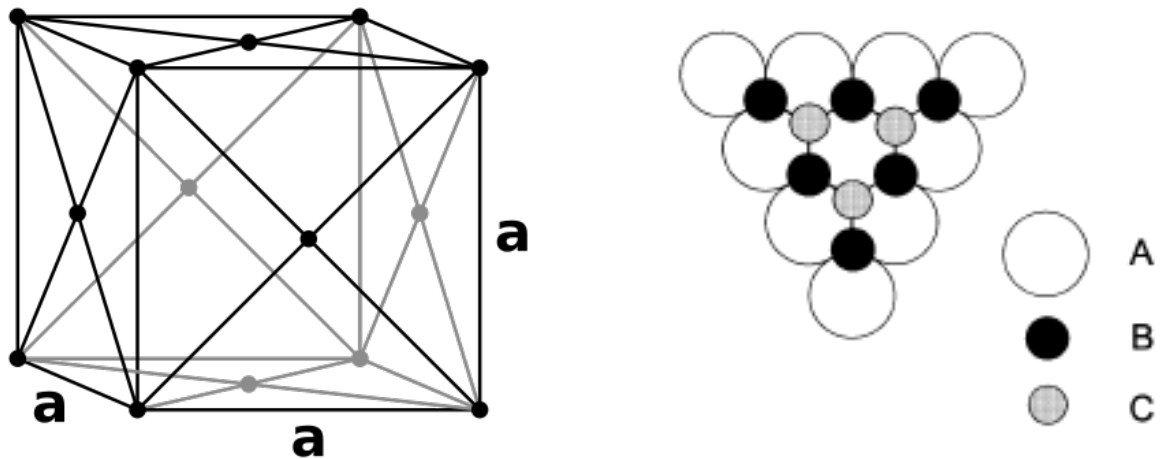


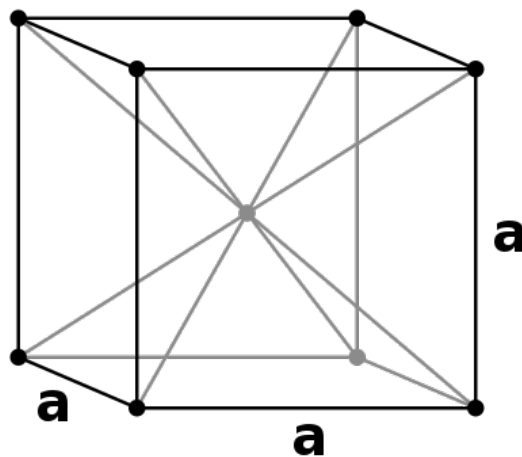
Figure 1.2.2: face-centered cubic structure



(a) unit cell of fcc structure [16]

(b) stacking sequence in fcc crystal close-packed direction [15]

Figure 1.2.3: body-centered cubic structure[17]



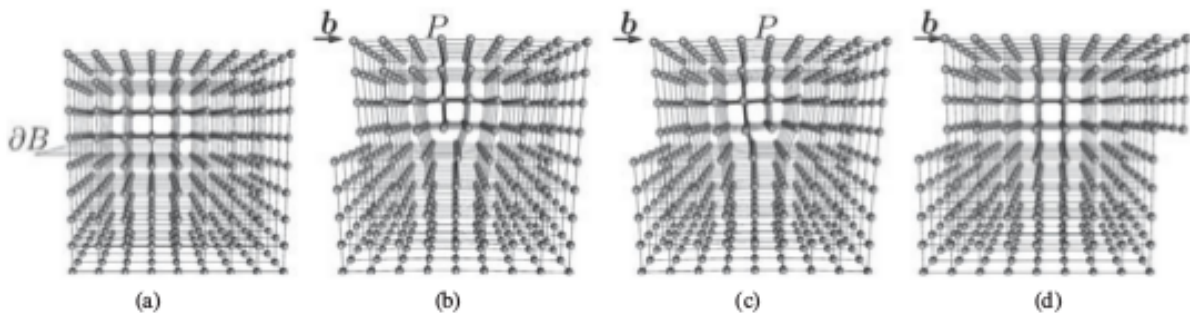
### 1.3 Defects in metals

Real crystals differ from the perfect crystal structures described in the previous section in various ways. Firstly, real crystals cannot be infinite and must end with a free surface or an interface with another material. Secondly, real crystals exhibit different defects in the structure, which are deviations from the perfect crystal lattice. Defects can be classified according to their characteristic dimensions as point defects, line defects, planar defects and volume defects. The amount and arrangement of microscopic defects often plays a crucial role in macroscopic behaviour of materials, for example various defects are responsible for the discrepancy between the theoretical and experimental value of shear stress needed to plastically deform a material [15].

### 1.3.1 Dislocations

Dislocations are line defects through a crystal that denote a region where there is a systematic local mismatch between two layers of atoms [2]. The concept of dislocations was introduced to explain the fact, that the theoretical strength of materials calculated with the model which assumed, that in the case of plastic deformation, an entire plane of atoms slips over an underlying layer, was orders of magnitude higher than the experimentally observed value. Simple dislocations can be illustrated by an example in Figure 1.3.1, which describes the plastic deformation of a crystal under shear. A crystal is divided into two sides by a plane  $\partial B$ . Shear stress is imposed on the top side of the material. This causes a local slip of atoms that propagates from left to right. The region of slipped atoms ends with an extra half layer of atoms P. The line where the layer P ends is the dislocation and it separates the slipped and non-slipped parts of the crystal. Because the slip and the movement of the dislocation is gradual and local, smaller shear stress is needed to cause a plastic deformation [15].

Figure 1.3.1: Slipping of a crystal through the movement of a dislocation [2]



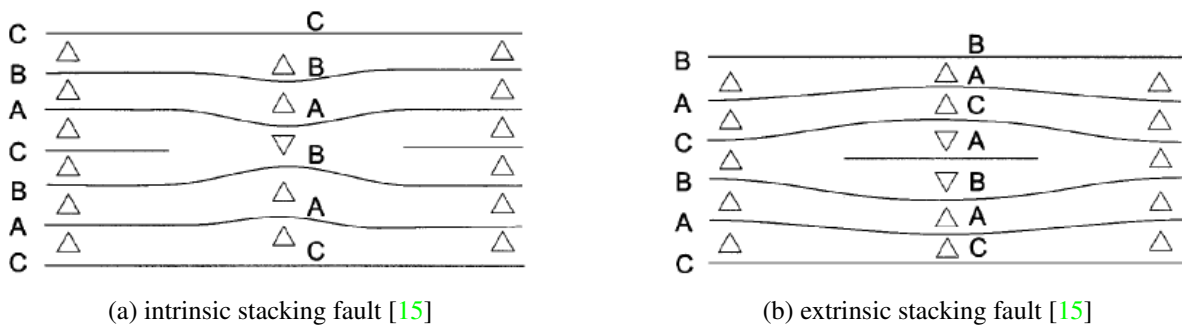
### 1.3.2 Stacking faults

Stacking faults are planar defects that consist of regions with locally wrong stacking sequence as compared to the rest of the crystal [15]. Stacking faults arise from the fact, that for close-packed direction, there exists two possible configurations to stack a layer of atoms on top of another. For example in fcc metal, the stacking sequence of atomic planes in close-packed direction is ABCABC. Geometrically a hexagonal layer of atoms laying on layer B can be in both A and C configurations, giving the rise to the possibility of locally hcp-like structured layers. The two types of stacking faults in fcc metals can be visualized by creating or removing a layer of atoms in a crystal. If a layer of atoms is removed, the resulting configuration is called an intrinsic stacking fault and creates two layers of atoms with hcp-like coordination. If a layer of atoms is added, the configuration is called an extrinsic stacking fault and creates one layer of atoms with hcp-like coordination. The introduction of stacking faults disrupt the structure of the crystal and thereby increase the energy of the system.

### 1.3.3 Grain boundaries

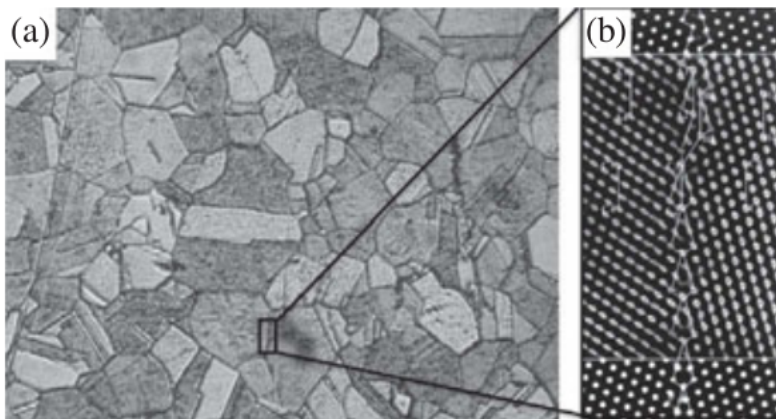
In principle, a perfect monocrystal periodic in every dimension is the lowest energy configuration for metals, including copper. Because of the way crystalline materials form, typically

Figure 1.3.2: Stacking faults in fcc metals



through melting and resolidification, they very rarely form one big monocrystal as there are many nucleation site for the growth of crystal structure randomly distributed but instead they consist of small crystallites [15]. Those crystallites are monocrystals with different crystal orientation and are separated by planar crystal defects called grain boundaries. An example of a copper polycrystal can be seen in Figure 1.3.3.

Figure 1.3.3: Copper polycrystal. a) shows the large-scale structure of the polycrystal and b) shows the magnification of a grain boundary, where local lattice mismatch can be seen [2]



It has been shown, that grain boundaries found in polycrystals and triple junctions act as stress concentrators [18], which can cause dislocation nucleation from those regions which could cause surface modification.

## 2 Methodology

### 2.1 Classical molecular dynamics(MD)

Computer simulations can be divided into several levels, depending from the time and length scales under investigation. For example, quantum mechanical methods can be used to investigate the systems consisting of several, up to hundred atoms to obtain precise description of the system. To simulate larger systems, some simplifications are already needed to avoid excessive cost of computational resources. Although well-established theories about atomistic interactions exist, the so-called first-principles or ab initio calculations based on quantum mechanics are not sufficient to study phenomena in materials emerging in very different time-and length scales. For that reason, classical molecular dynamics has the middle-ground: it still allows to take the atomic structure of material into account, while being computationally less intensive.

Classical molecular dynamics is a simulation technique developed in the 1950s [19], that simulates the motion of each individual atom separately. Atoms are treated as point particles and they interact through an empirically defined potential energy function usually abbreviated simply as the potential, which is a function of the coordinates of all atoms. From this potential, inter-atomic forces are derived, which are used to numerically solve Newton's equations of motion for all of the atoms:

$$m_i \frac{d^2 \vec{r}_i}{dt^2} = -\nabla U_i(\vec{r}_1, \vec{r}_2, \dots, \vec{r}_N) \quad i = 1 \dots N \quad (2.1.1)$$

From the resulting trajectories, along with the velocities and forces at each timestep, ensemble average of a physical quantity under interest can be found using the ergodic hypothesis from the time average over the course the simulation of the respective physical quantity. This assumes that the system is in an equilibrium state, meaning that the physical quantities under interest should fluctuate around a mean value without a drift. For example, in this case the temperature of the system can be written as the time-averaged vibrational kinetic energy of the system: [2]

$$T = \frac{2}{3Nk_B} \left\langle \sum_{i=1}^N \frac{1}{2} m_i |v_i^{rel}|^2 \right\rangle \quad (2.1.2)$$

Where  $v_i$  is the velocity of the atom  $i$  relative to the center of mass of the system. It is useful to define the instantaneous temperature  $T_{inst}$  which will fluctuate around this average:

$$T_{inst} = \frac{2}{3Nk_B} \left( \sum_i^N \frac{1}{2} m_i |v_i|^2 \right) \quad (2.1.3)$$

An MD simulation usually corresponds to a set of external physical conditions, so that the concept of statistical mechanics ensembles can be used [20]. Microcanonical(NVE) ensemble corresponds to an isolated system with constant number of particles(N), constant volume(V) and energy(E). As a real physical system is rarely isolated from its surrounding, considering a system in thermal contact with its surroundings is often physically more realistic. An ensemble representing this kind of system is called the canonical(NVT) ensemble, which means that the number of atoms, volume and the temperature of the system is conserved. In practice, MD algorithms used in MD to sample a system in a canonical ensemble are also used for changing the temperature during the course of an MD simulation. One of the most widely used algorithms to sample the NVT ensemble is the Nose-Hoover thermostat [21, 22], which is also used in present work. In their formulation, the Hamiltonian of the system is extended so, that a fictitious particle with one-dimensional momentum  $P$  and mass  $M$  is coupled to the system. It can be show the equations of motion for the system can be rewritten thus:

$$m_i \frac{d^2}{dt^2} \vec{r}_i = \vec{f}_i - \gamma m_i \frac{d}{dt} \vec{r}_i$$

Where  $\gamma = \frac{P}{M}$  is the “damping factor” which can be both positive and negative and  $\vec{f}_i = \nabla U_i(\vec{r}_1, \vec{r}_2, \dots, \vec{r}_N)$  is the force on the  $i$ -th particle. The differential equation for  $\gamma$  can be written so:

$$\frac{d}{dt} \gamma = \frac{1}{\tilde{M}} (T_{inst} - T)$$

Where  $T_{inst}$  is the instantaneous temperature at a moment in time and  $\tilde{M} = 3k_B \frac{M}{N}$ . It can be seen, that if  $T_{inst} > T$ ,  $\gamma$  will increase and hence increase the damping until the target temperature is reached, and vice-versa. This algorithm has one free parameter  $M$  - the “mass” of the virtual particle. This parameter has to be chosen according to the system at hand - too small mass leads to wild fluctuations in temperature of the system, while too large of a mass leads to too little coupling between the atomic system and the thermostat, which leads to bad temperature control.

### 2.1.1 Numerical integration schemes for MD simulations

The numerical scheme to integrate the resulting equations of motion have to meet certain criteria: As a result of this discretization, certain qualities of equation (3.1.1) have to be preserved. First, the integration scheme has to conserve the total energy of the system as does (3.1.1). Second, it has to be time-reversible and third, it has to be symplectic, which means that the phase space volume contained by the system must be reserved(Liouville’s equation must hold).[2] There are many numerical schemes that satisfy those requirements, for example second-order integration schemes Leap-Frog [23], and Velocity-Verlet[24, 25], the latter of which is used throughout present work and is given below in Algorithm 2.1.

To be able to simulate an atomic phenomenon, timestep size used must usually be at least an order of magnitude smaller than the smallest characteristic time scale of the phenomenon studied. For metals, this timescale can be estimated using the Debye frequency of the metal [2], which roughly corresponds to the fastest vibrations of the atoms due to thermal motion:

---

**Algorithm 2.1** The Velocity-Verlet algorithm

---

1. Assign starting coordinates and velocities  $\mathbf{r}_i(t=0)$ ,  $\mathbf{v}_i(t=0)$  to each atom with timestep  $\Delta t$
  2. Derive forces from interatomic potential for each atom:  
$$\mathbf{F}_i(t) = -\nabla_i V(\mathbf{r}_i(t))$$
 with acceleration  $\mathbf{a}_i(t) = \frac{\mathbf{F}_i(t)}{m_i}$
  3. update coordinates  $\mathbf{r}_i(t + \Delta t) = \mathbf{r}_i(t) + \mathbf{v}_i(t) \Delta t + \frac{1}{2} \mathbf{a}_i(t) \Delta t^2$
  4. calculate acceleration at timestep  $t + \Delta t$ :  $\mathbf{a}_i(t + \Delta t) = -\nabla V_i(\mathbf{r}_i(t + \Delta t))$
  5. update velocities:  $\mathbf{v}_i(t + \Delta t) = \mathbf{v}_i(t) + \frac{\mathbf{a}_i(t) \Delta t + \mathbf{a}_i(t + \Delta t) \Delta t}{2}$
  6. update timestep  $t = t + \Delta t$   
repeat until necessary conditions are met or last iteration  $t_{max}$
- 

$$\omega_D = v_s \left( \frac{3N}{4\pi V} \right)^{\frac{1}{3}}$$

where  $v_s$  is the speed of sound in that metal and  $\frac{N}{V}$  is the number density of atoms in the metal. For copper, which has lattice constant of 3.6 and speed of sound of  $3900 \frac{m}{s}$ , this frequency is about one cycle per 0.1 ps. This means, that the timestep size should be below 10 fs. On one hand, too small of a timestep is computationally expensive while too large of a timestep leads to numerical errors and total energy drift. In this thesis, timestep size is chosen everywhere to be 2 fs, to ensure proper dynamics for non-equilibrium configurations.

### 2.1.2 Embedded atom method(EAM) and EAM potentials

As the time evolution of the system in an MD simulation is directly governed by the interatomic potential used, the choice of this potential is of utmost importance. A great variety of interatomic potentials exist which differ greatly in their accuracy, computational cost and parametrization principles. Depending on the nature of the problem, different energy terms for the potential might be needed, for example to account for chemical bond stretching and bending, and also due to long-range Coulombic forces. As this thesis concentrates on simulating copper which exhibits metallic bonding, most of these components are absent and it is possible to simulate the system using simple pair potentials or a more sophisticated versions to those, like Embedded Atom potentials [26]. In the EAM formulation, the total potential energy of the system is given by:

$$E = \frac{1}{2} \sum_{ij, i \neq j} V_{ij}(r_{ij}) + \sum_{\alpha} U_{\alpha}(\rho^{\alpha}) \quad ,$$

where  $V_{ij}$  is the energy of pairwise interaction of particles with indices  $i, j$  and  $r_{ij}$  is the distance between atoms  $i$  and  $j$  while  $U_{\alpha}$  is the energy associated with embedding an atom to the

environment governed by the functional  $\rho^\alpha$ , which itself is a function of all the coordinates of the atoms. There are different physical explanations how to justify different parametrizations of functionals  $U_\alpha$  and  $\rho^\alpha$ , but the simplest explanation is that  $V_{ij}$  is the Coulombic interaction between the atomic cores of atoms  $i, j$  and that  $U_\alpha(\rho^\alpha)$  is the energy needed to embed an atom in a background electron density  $\rho^\alpha$ , which is simply taken as the linear superposition of electron densities from neighbouring atoms. This assumes that the contribution to the electron density  $\rho^\alpha$  from a neighbouring atom depends only on the distance from that atom, with no angular dependence, which is not strictly true. Yet it is possible to get satisfying results with this method when simulating elements with filled d-orbitals, like copper which do not exhibit covalent or directional bonding[27]. Functionals  $U_\alpha$  and  $\rho_\alpha$  are fitted from quantum mechanical methods like Density Functional theory or from experiment, to reproduce as closely as possible the physical properties of interest of the system under study [2, 27]. In current work, the EAM potential for copper by Mishin et al. is used [28]. It has been shown that this potential realistically models copper structures far from equilibrium and correctly predicts the elastic properties, cohesive energy and stacking fault energies of copper [29, 30] and has been previously used for molecular dynamics study of elastic and inelastic deformations of polycrystalline copper [31].

### 2.1.3 Atomic stress calculations

The symmetric per-atom instantaneous stress tensor in molecular dynamics for atom  $i$ , counting only pair-wise potential energy terms can be calculated[32, 2]:

$$\mathbf{S}_i = -\frac{1}{V_i} \left( m_i \vec{v}_i \otimes \vec{v}_i + \frac{1}{2} \sum_{j=1}^N \vec{f}_{ij} \otimes \vec{r}_{ij} \right) ,$$

where  $V_i$  is the volume of atom  $i$ ,  $\vec{v}_i$  is the velocity of atom  $i$ ,  $\vec{f}_{ij}$  is the pair-wise interatomic force that atom  $j$  exerts on atom  $i$  and  $\vec{r}_{ij}$  is the position vector of atom  $i$  with origin at atom  $j$ . The per-atom stress tensor consists of two components - first one is the momentum flux associated with the vibrational kinetic energy of the system (it is assumed, that the center of mass velocity of the system is 0). The second one is the contribution from interatomic forces associated with the potential energy of the system. As an instantaneous quantity, suitable time averages in an equilibrated system must be taken to obtain a suitable stress distribution cleared of thermal noise. To obtain macroscopic stress in a system, suitable time and volume average must be taken. It has been shown[33] that the macroscopic stress tensor acquired in this way reduce to the continuum Cauchy stress, if sufficient time and space averages are performed. Let it also be noted, that most MD programs implement the atomic stress in a *stress \* volume* formulation, as the volume of an atom is not well defined for a non-homogenous deformed solid or liquid [34] and also for the case of non-periodic system. It is up to the user to define a suitable atomic volume for the model under study. One useful quantity to analyze the failure of a material is the Von Mises stress. The Von Mises stress for a point in a system can be calculated from the stress tensor components as so [35]:

$$\sigma_{vm} = \sqrt{(S_{11} - S_{22})^2 + (S_{22} - S_{33})^2 + (S_{33} - S_{11})^2 + 6(S_{12}^2 + S_{23}^2 + S_{31}^2)}$$

The yield criteria for metals is connected to the Von Mises stress, as the metal starts yielding at some critical value of  $\sigma_{vm}$ . This can be physically interpreted as the necessary condition under

which the elastic energy of distortion reaches a critical value[36, 37]. Another useful aspect of Von Mises Stress is that it reduces the stress tensor components into a scalar, which, from a practical point of view, is often easier to analyze.

## 2.1.4 Potential cut-off value

In principle, if one has to take into account all interactions between all atoms, the computation time in a MD simulation scales with  $n^2$  where  $n$  is the number of particles in the system. As most interaction terms in MD are short range, a cutoff value  $r_{cut}$  is used in most models, which simply means that the potential is truncated for atom pairs further from each other than  $r_{cut}$ . One possibility to avoid the artificial step in energy and force when an atom moves further than  $r_{cut}$  is to modify the interatomic potential  $U(r)$  as follows:

$$U_1(r) = U(r) - \left. \frac{dU(r)}{dr} \right|_{r=r_c} \cdot (r - r_c)$$

Then, the new potential  $U_1(r)$  and force  $f_1(r)$  tend smoothly to 0 when  $r \rightarrow r_{cut}$ . Obviously this changes the parametrization of the potential, so care should be taken to choose the cut-off value big enough for the correction term to become small enough.

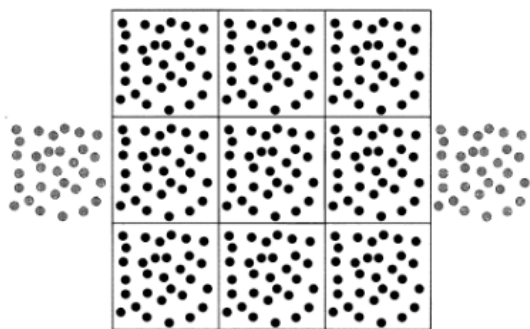
## 2.1.5 Periodic boundary conditions

As only systems containing a limited number of atoms can be simulated with molecular dynamics, special care must be taken with the choice of boundary conditions, if one wishes to simulate a bulk material or simply a material infinite in one or more directions. For that effect, periodic boundary conditions are most often used. Periodic boundary conditions mean, that the simulation box containing the atoms is taken to be a unit cell of the system and is repeated infinitely in each direction and all the interactions between atoms in all images, even the interaction of an atom with it's own periodic image are taken into account. This somewhat complicates the simulation process, as the potential energy for each atom has to be calculated as an infinite sum, but as most interatomic potentials use a cut-off value, this is rarely a problem. Special care has to be taken when the potential contains long-range terms, like electrostatic interactions, other methods have to be used in that case[38], but in current work only short range interatomic forces are present. As PBCs can create unwanted artifacts from for example the interaction of images of extended effects, care must be taken to ensure that the effect of those is minimized. Besides bulk material, 1D and 2D systems, for example nano-wires and surfaces can also be simulated with periodic boundary conditions - in that case, one has to set the simulation cell size in a non-periodic direction greater than the cut-off value of the used potential.

## 2.1.6 Equilibration

In MD simulations, an equilibration is called a simulation during which, the conditions imposed on the material, for example temperature and pressure, are not changed and the system is allowed to dynamically evolve according to the assigned potential function for some time to allow

Figure 2.1.1: Illustration of periodic boundary conditions. The original cell and its 10 images in 2D are depicted [20]



the system to relax to a lower energy through thermal fluctuations [38]. This is necessary, because very rarely the conditions can be changed as slowly as needed for the system to remain in equilibrium and is often done before and after a simulation with changing conditions or to create a physical equilibrated configuration out of initial created state. Achieved equilibrium state is indicated by several factors, like plateaued potential energy and reasonably small temperature and pressure fluctuations, although no strict criteria exist to determine when the structure has reached sufficiently good equilibrium state. Another possible measure of achieved equilibrium is the velocity autocorrelation function(VCF) [2]:

$$VCF(t) = \sum_{i=1}^N \vec{v}_i(t=0) \cdot \vec{v}_i(t)$$

Where  $\vec{v}_i$  is the velocity of atom  $i$  and the sum is taken over all  $N$  atoms. For the system to be equilibrated, the VCF has to go to 0, indicating that the system has lost its “memory” of the initial state.

## 2.1.7 Simulated annealing

Simulated annealing [39] is a simulation technique to probe the potential energy landscape of the system under study and to further relax a structure with many possible equilibrium positions and “stuck” in a not sufficiently good local minimum. Annealing consists of three steps:

- Elevating the temperature of the system to some higher value so that the kinetic energy of the atoms would increase sufficiently to overcome the energy barriers of the local minima
- Run an equilibration at the elevated temperature to stabilize the system
- slowly decrease the temperature back to working temperature

Due to thermal fluctuations, the states of the system with energy  $E$  are visited with a probability proportional to  $\exp\left(-\frac{E}{kT}\right)$ . If the system is heated, it can freely hop between different minima, spending more time in deeper ones. As the system is cooled, atoms settle again into local minima positions, but more probably into minima which correspond to a better (lower potential energy) structure. The temperature lowering time must be as big as possible, otherwise the local minima are not correctly sampled.

## 2.2 Analysis methods of crystalline structures

### 2.2.1 Centrosymmetry parameter(CSP)

As mentioned in chapter 1, defects in crystal lattice play an enormous role in material properties, and as such, it is important to be able to extract the information about defects from the data of the sample under study. As MD methods do not keep track of defects internally, it is necessary to apply algorithms that do so as part of the post-simulation processing [40]. Although there are many ways to analyze possible defects in the sample studied, here are presented two methods, that are used in this thesis: analysis of Centrosymmetry Parameter, usually abbreviated CSP, and Common Neighbour Analysis. Centrosymmetry Parameter assigns a scalar to each atom by looking at it's nearest neighbours :

$$CSP = \sum_{i=1}^{N/2} \left| \mathbf{r}_i + \mathbf{r}_{i+\frac{N}{2}} \right|^2$$

Where  $N$  is the number of neighbours for each atom, for fcc crystals  $N = 12$ . Here  $\mathbf{r}_i$  and  $\mathbf{r}_{i+\frac{N}{2}}$  are position vectors from the central atom to a pair of neighbours, which lie symmetrically with respect to the central atom, hence the notation  $i$  and  $i + \frac{N}{2}$ . CSP is nearly 0 for atoms in their regular positions corresponding to a perfect crystal and is non-zero for atoms near or part of a defect. One of the advantages of CSP is that it has rotational symmetry, that is it depends only on the neighbourhood of an atom, not on the orientation of particular crystal. The disadvantages include not being able to distinguish between different defects and sensitivity to noise due to thermal displacements of atoms from their equilibrium sites, which means, that at higher temperature the distributions of CSP of fcc atoms and defect atoms, like in stacking faults, begin to overlap.

### 2.2.2 Common Neighbour Analysis(CNA)

Because of reasons outlined previously, more robust crystal structure analysis methods, like Common Neighbour Analysis [41, 42] is required and is used extensively in current work. In CNA a characteristic signature of an atom is constructed from the information of bonds connecting an atom with it's neighbours. Two atoms are said to be bonded if the distance between them is small than some cut-off value  $r_c$ . For fcc crystals, this is usually taken to be between first and second neighbouring shell [40] :

$$r_c = \frac{1}{2} \left( \frac{1}{\sqrt{2}} + 1 \right) a \approx 0.854a$$

Where  $a$  is the lattice constant of the crystal. To assign a particular atom a configuration type, three characteristics are calculated for the neighbours of an atom in interest - the number of neighbours the atom and it's neighbour have in common  $n_1$ , the total number of bonds between those common neighbours  $n_2$  and the number of bonds in the longest chain connecting those atoms  $n_3$ . From this, a characteristic signature  $(n_1, n_2, n_3)$  is obtained and compared with

reference signatures of different structure types, assigning a structure type to the atom of interest. In current work, three different atom types are of most interest - undefined structure(type 0, denoted with color grey throughout current work) which is assigned to surface and grain boundary atoms, fcc structure, which is assigned to atoms in their perfect lattice configuration(type 1, denoted with color green) and hcp, which denote atoms part of a stacking fault with hcp-like structure(type 2, denoted with color red).

### 2.2.3 Coordination Analysis

Coordination analysis calculates the number of neighbours an atom has within a given cut-off value  $r_{cut}$ , meaning in a volume  $\frac{4}{3}\pi r_{cut}^3$  around the atoms. This is useful for analyzing the local crystal of the material, as atoms part of a defect tend to have a lower coordination number. Another trivial but useful property of the coordination number and one that is used extensively in current work, is that surface atoms have lower coordination numbers than the surface atoms. This allows for the identification of the surface atoms even in the case of deformed geometries. A concept closely related to the coordination number is the radial pair distribution function  $g(r)$ , which is a measure of the distances between atom pairs and shows the number of atoms pairs whose distance lies in the narrow range of  $(r; r + dr)$ . The maximum of the RDF corresponds to the most probable distance between atom pair, which for fcc metals is the nearest neighbour distance of  $\frac{\sqrt{2}}{2}a$ , where  $a$  is the lattice constant. Because of this property, the radial pair-distribution function can be used calculate the atomic radii and volumes even in the case of deformed geometries.

## 2.3 Used software

The main software package used in current work is Large-Scale Atom/Molecular Massively Parallel Simulator(LAMMPS)[43, 44] It a a free open-source software written in the C++ language that is specifically designed to conduct large-scale parallel simulations through its message-parsing-interface(MPI) and spacial decomposition the simulation domain between processor cores. For molecular dynamics simulations, lammmps offers the capability through implemented potentials to simulate metals, semiconductors, polymers and liquids. As a mainly computational tool, LAMMPS offers little pre-or post processing capabilities, meaning often the input geometry and analysis of the results have to be provided by other means. Almost 80% of the code base of LAMMPS is user-written and it has an active user-base. As LAMMPS itself does not offer capabilities for visualizing the simulation data, another software named OVITO is used for that effect. [45] OVITO is a free 3D analysis and visualization software, that is compatible with the output data of LAMMPS. OVITO features visualization and manipulation of simulation data, as well as a number of built in modifiers and analysis tools used extensively in current work, like coordination analysis and radial distribution function calculations, common neighbour analysis, centrosymmetry calculations and visualization of custom simulation data from LAMMPS, for example atomic stress tensor components. Comsol Multiphysics is a commercial Finite Element Method software for various physics and engineering applications. Comsol Multiphysics is often used to study coupled systems described by set of coupled partial differential equations. In current work Comsol is used to electrostatics and structural mechanics problems. To move between the atomistic simulation domain described by molecular dynamics

and implemented in LAMMPS and the continuum representation modeled with Comsol, Python script were developed and implemented for the use in current work.

## 2.4 The electric field distribution at the material surface

In classical electrostatics theory it is shown that the electric field near a conducting surface is always parallel to the normal vector of the surface and the surface charge density  $\sigma$  induced on the surface can be calculated as  $\sigma = \frac{E}{\epsilon_0}$ , where  $E$  is the electric field right above the surface and  $\epsilon_0$  is the permittivity of vacuum. The electric field distribution itself depends on the geometry of the surface and the general principle is that the electric field is locally increased near the places on the surface with smaller curvature radius. It can be shown, that the electrostatic force acting on a surface element  $S$  can be calculated as:

$$F = pS = \frac{\epsilon_0 E^2}{2} S \quad (2.4.1)$$

[46]

Where  $E$  is the local electric field above the surface element  $S$ . In atomistic framework however, the forces acting on each atom must be defined and for that effect, the induced partial charge and induced dipole moments belonging to each surface atom have to be defined, to be able to calculate the force exerted on the surface by the external electric field. This can be done in the framework of Density Functional Theory [47], although further models should be devised to divide the resulting charge density between atoms. Similar results could be achievable within the recently developed Electrostatic Interaction Model by Jensen and Jensen [48], which has been used to study the effects of the external electric field on silver nano-wires [49], but is unusable in present work because of computational limitations by large system size and simulation lengths. In present work, a different approach consolidating the continuum model simulated by FEM and atomistic MD calculations is devised. The steps needed for this approach are as follows:

1. Detect the surface atoms on which to apply the electrostatic force.
2. Smooth the position of the surface atoms to be create a mathematically smooth surface
3. calculate the electric field electrostatic stress distribution on that surface using Finite Element Method
4. use the resulting stress distribution to apply electrostatic force on the surface atoms.

### 2.4.1 Detection of the surface atoms

To be able to correctly identify the surface atoms, the surface detection algorithm needs to have the following properties:

- As shown in electrodynamics textbooks [46] static electric fields do not penetrate further into the surface of a conductor more than 1 atomic layer or around 2 Å. This means that the algorithm has to be able to select only the topmost layer of the sample.
- Secondly, the algorithm must cover the whole surface and not leave any holes, as this would create a situation where some of the surface atoms have artificially greater force exerted on them and some of the surface atoms have no electrostatic force exerted on them
- Thirdly, it should be able to find the surface atoms even on rough surfaces and have minimal false-positives of bulk atoms. False positives in the bulk mean that some of the bulk atoms have an artificial force exerted on them as if they were part of the surface and as the coordination number is more probably low for bulk atoms that are part of a material defect, this will lead to an artificial force exerted on the defects.

In present work, coordination analysis is used for finding the surface atoms. The motivation for this is simple in principle - surface atoms should have, on average, half the number of neighbours of bulk atoms. The sphere around an atom in where the coordination number is calculated is taken to be as large as possible, to reduce the error due to a non-smooth surface. For implementation reasons this cannot be taken to be larger than the cut-off value of the used potential, which in this work is 5 Å and which is also taken as the radius of the sphere. In theory, it would be possible to calculate exactly the coordination number of an atom belonging to a surface aligned with a specific crystallographic planes, but due to thermal fluctuations and the fact that the surface of the system under study in present work has randomly oriented grains, no such number can be rigorously calculated, although it can be empirically chosen to meet the aforementioned criteria for a particular system.

## 2.4.2 Creating a smooth surface for electric field calculations

As the surface detected by the method described in the previous section is inherently rough, it is not possible to simply interpolate a smooth surface through the coordinates of the surface atoms and smoothing of the surface atoms positions is necessary. For that effect, the following method is used: the whole length of the surface is divided into 1D bins with thickness  $d$ . As the system under study in current work is periodic in one direction, this 1 dimensional discretization is sufficient, if that were not the case, rectangular boxes with dimensions  $d \times d$  could be used. For each slice, the coordinates of the surface atoms in that slice are averaged and used to create an interpolation point with coordinates:

$$\vec{r}_n = \frac{\sum_i^N \vec{r}_i}{N}$$

Where  $\vec{r}_n$  is the position vector of the point corresponding to the  $n$ -th slice with  $N$  atoms. This process creates a set of points through which a surface can be interpolated. The bin thickness  $d$  is a crucial parameter in this method. If the bin size is chosen too large, the number of points created is too small to interpolate through, which makes the resulting surface overly smooth, thereby diminishing the effect of field enhancement. On the other hand, if the bin size is too small, the number of points created is too large, which leads to unrealistically rough

surface creating too high field enhancement. The simulations to test for the proper value of  $d$  is presented in Section 3.1 and the results of the comparison of different bin sizes is presented in Section 4.1.

### 2.4.3 Calculating the electric field

The smooth surface can be extrapolated through the points obtained by the method described in the last paragraph. Piecewise-cubic splines are used to interpolate a smooth mathematical surface through the interpolation points. To calculate the electric field distribution suitable boundary conditions must be imposed. To calculate the electric field, the resulting surface was chosen as an equipotential (Dirichlet boundary condition) and for definiteness was chosen to be  $\varphi_{surface} = 0$ . Von Neumann boundary condition was chosen on the top boundary of the simulation domain with the electric field defined on the boundary as the reference value of  $\vec{E} = E_0 \hat{y}$  where the  $y$ -direction is taken to be the vertical direction. The boundary conditions on the sides of the simulation domain were chosen as  $\vec{n} \cdot \vec{E} = 0$  which means that the electric field near the sides of the simulation domain is parallel to them. The electric potential everywhere with the chosen boundary conditions can be found by numerically solving the Laplace equation for the electric potential:

$$\nabla^2 \varphi = 0 \quad (2.4.2)$$

From the solution, the electric field  $E = -\nabla \varphi$  can be found at each point of the simulation domain and particularly on the material surface.

### 2.4.4 The effect of electrostatic forces on the surface atoms

Let us view a surface element corresponding to the slice with width  $d$ , on which there is defined outwards electrostatic stress  $p = \frac{\epsilon_0 E^2}{2}$ , and normal vector components which are not necessarily constant in the slice. Let  $\alpha$  be the angle between  $\vec{n}_y$  and  $\vec{n}$ . The total electrostatic force acting on the surface element is:

$$\Delta F = \Delta p S$$

where  $S$  is the area of the surface element and  $\Delta p$  is the average stress on the surface. The components of the force:

$$\Delta F_y = \Delta F \cos \alpha = \Delta p S \cos \alpha = \left( \frac{1}{d} \int_{x_0}^{x_0+d} p \, dx \right) \frac{zd}{\cos \alpha} \cos \alpha = \left( \frac{1}{d} \int_{x_0}^{x_0+d} p \, dx \right) zd$$

$$\Delta F_x = \Delta p S \sin \alpha = \left( \frac{1}{d} \int_{x_0}^{x_0+d} p \, dx \right) \frac{zd}{\cos \alpha} \sin \alpha = \left( \frac{1}{d} \int_{x_0}^{x_0+d} p \, dx \right) zd \frac{n_x}{n_y}$$

where  $n_x = \int_{x_0}^{x_0+d} n_x(x) \, dx$  and  $n_y = \int_{x_0}^{x_0+d} n_y(x) \, dx$  are the average normal vector components in that particular slice.

For each surface element the stress over that element and the normal vector components have to be averaged. Because stress depends on the electric field as  $p \sim E^2$ , care should be taken not to average the electric field and then calculate the stress from this average field. To get the force on each atom in a particular slice, the total force acting on the element is divided with the number of atoms corresponding to that slice,  $\vec{f}_a = \frac{\Delta \vec{F}}{N}$  and applied equally to all atoms in that particular slice.

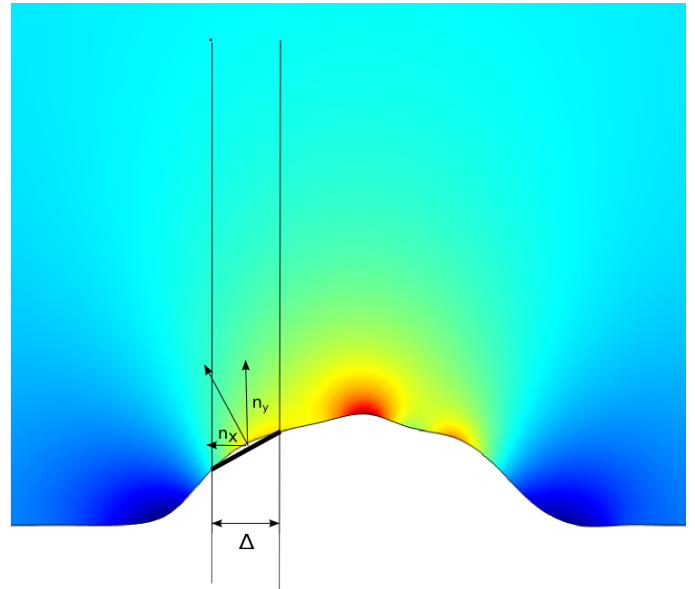
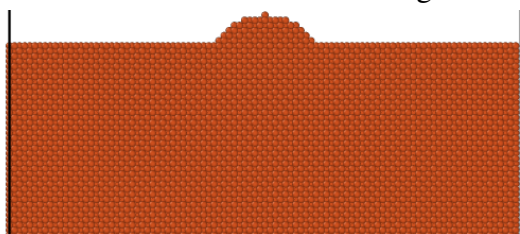


Figure 2.4.1: Force components acting on surface element.  $\Delta S = z\Delta$   
The colors represent the electric field distribution corresponding to a particular  $d$  and can be ignored for the time being.

## 3 Simulations

### 3.1 Test case for the surface construction and electric field distribution

Figure 3.1.1: Test case geometry



To test the methods developed and described in Section 2.4, a small test case was prepared. The test geometry consists of thin slab with width of  $50a$ , thickness of  $10a$  and height of  $25a$ , where  $a$  is the lattice parameter of copper,  $a = 3.615\text{\AA}$ . A protrusion was created on the surface in the form of a section of a cylinder with curvature radius of  $6a$  to best mimic the geometry of the sample under study, which is periodic in the  $z$ -direction. The interpolation points for surface reconstruction were found as described in Section 2.4.2 using custom-written Python scripts with two different bin sizes:  $d_1 = 1a$  and  $d_2 = 0.5a$ . The resulting interpolation points were exported into Comsol and a smooth surface was interpolated through the points using piece-wise cubic splines. The electric field distributions were calculated with Comsol using the following boundary conditions: the surface of the system was assume to be an equipotential, which for definitiveness was taken to be  $\varphi_{surface} = 0\text{ V}$ . Constant electric field was defined on the top side of the simulation domain, which was taken as the reference electric field value of  $E = 100 \frac{\text{MV}}{\text{m}}$ . The geometries and results of this test case study is presented in Section 4.1.

## 3.2 Preparing the sample

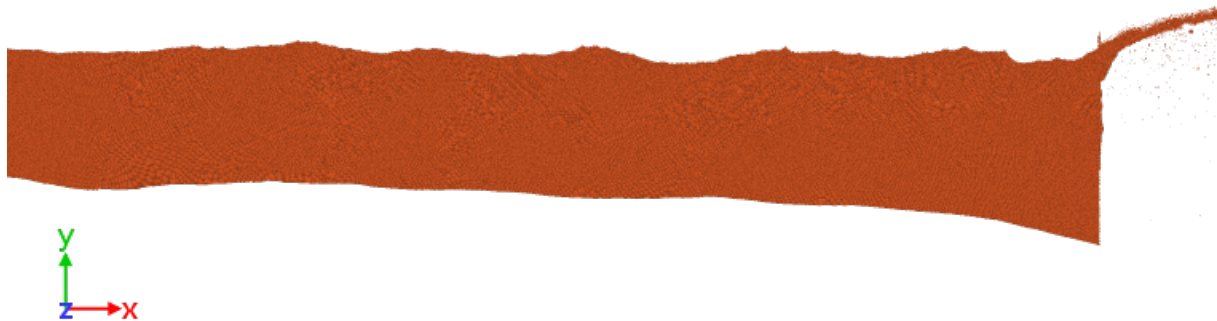
### 3.2.1 Setup and initial geometry

The system that is used in this work originates from a previous simulation conducted in University of Helsinki Department of Physics by Ossi Saresoja *et al.* as described here: [50]. The authors simulated explosive welding process between monocrystal copper and iron plates, after

which, polycrystalline structure with 10 – 20 nm grain size appeared in both materials. The starting point for simulations in current thesis is the copper part of the material, with iron atoms removed. The system partly resembles a material after a breakdown event, because both vacuum breakdown and explosive welding essentially cause a shock wave to propagate from the material surface, causing massive plastic deformation. The sample consists of about 7.65 million copper atoms forming a thin slab about 400 nm long in x-direction, 50 nm wide in y-direction and 4 nm thick and periodic in the z-direction. As the snapshot of the sample is taken right after the welding process and is in a highly compressed state, measures have to be taken to release the initial stresses in the material and to reduce the amount of defects present. For this purpose, three methods are used in this thesis to acquire a sample that could be used in further simulations:

1. Perform energy minimization on the system at 0 K using Nonlinear Conjugate Gradient(CG) minimization scheme
2. raise the temperature of the system to 300 K and perform equilibration.
3. Take the equilibrated structure acquired in previous section, anneal it to a higher temperature and then slowly reduce the temperature back to 300 K.

Figure 3.2.1: Initial sample after the explosive welding simulation. On the right the jet of atoms from the welding simulation can be seen.



### 3.2.2 Energy minimization

To perform minimization, the atoms forming the jet were removed, as it consists of evaporated atoms with no structure of interest. The remaining sample consists of 6.85 million atoms: while further simulations were carried on a much smaller systems, This step was performed on a larger system to be able to identify interesting regions and to cut out an representative sample after the minimization. Boundary conditions in non-periodic x,y directions were not fixed, to allow free surfaces to form and thereby relax the internal stressed state of the system. Energy minimization was performed using Non-Linear Conjugate Gradient method [51] with quadratic line search algorithm, which tries to minimize the forces acting on the atoms, while making sure, that the total energy is not increased. As mentioned, the system is initially compressed,

so additionally the simulation box size was allowed to dynamically change in the periodic z-direction. The minimizer terminated because line-search parameter  $\alpha$ [51] reached 0, in other words, the minimizer could not reduce energy any further. This means, that the system had reached a local energy minimum, but this method offers no way to assess the quality of this local minimum except for crystal analysis.

### 3.2.3 Temperature ramping

After the initial minimization, a smaller sample was cut out of the system. The reasons for that were two-fold: first, only parts of the system exhibit an interesting polycrystalline structure and second, simulating the whole system would not be computationally feasible. The resulting sample consists of about 1.4 million atoms and is 100 nm long in the x-direction, 40 nm wide in y-direction and 4 nm thick in z-direction. The bottom layer was kept fixed during the temperature ramping, because without it, the system deformed undesirably during the simulation. To raise the temperature to 300 K, velocities were first created for the atoms corresponding to a temperature of 10 K with a gaussian profile. Because the velocity creating algorithm uses a random number generator, net linear and angular momentum have to be zeroed to prevent the sample as a whole from moving. After that, a Nose-Hoover thermostat was used to increase the temperature to 300 K with a simulation time of 100 ps. A Nose-Hoover barostat was also used to allow the sample to expand in the periodic direction and to keep the external pressure component  $p_{zz}$  at 0 Pa to allow thermal expansion during the preparation process.

### 3.2.4 Equilibration

After the temperature ramping, equilibration was performed for 100 ps with N-H thermostat and barostat, which kept the temperature at 300 K and  $p_{zz}$  at 0 Pa. This was necessary to let the system take equilibrium position before further processing. In MD simulations, an equilibration is called a simulation during which, the conditions imposed on the material, for example temperature and pressure, are not changed and dynamics is run for some time to allow the system to relax to a lower energy through thermal fluctuations. This is necessary, because very rarely the conditions can be changed as slowly as needed for the system to remain in equilibrium and is often done after a simulation with changing conditions.

### 3.2.5 Simulated annealing

To process the material further, simulated annealing [39] was used, to further remove the defects present and increase the size of the grains in the sample. Annealing consisted of 3 steps:

1. Raise the temperature to a high temperature. In this work, a temperature of  $0.8T_m$  is used, where  $T_m$  is the melting point of copper for this potential  $T_m = 1320K$ [28]. Simulations with lower end temperature showed inferior ability for defect reduction as compared to the  $0.8T_m$  case.
2. Keep the temperature elevated for some time.

3. Slowly reduce the temperature back to working temperature.

The idea of this procedure is to first increase the energy of the system so that it would overcome the energy barrier that confines it to its current local minimum of the potential energy surface and let it reach an equilibrium state corresponding to a higher temperature. The temperature was decreased with N-H thermostat to 300 K from  $0.8T_m$  during the course of 200 ps.

## 3.3 Applying the electric field

### 3.3.1 Constant electric field

After the equilibration and defect reduction steps the system was ready for applying force on the surface atoms modelling the effect of the applied electric field. The system boundaries in the  $x$ -direction were kept fixed during the simulation, meaning that atoms in the first two layers were allowed only to move in the  $y - z$  plane. This was done to avoid the geometry of the system from heavily distorting during the course of the simulation. This can also be physically justified by the fact, that in experimental conditions, the area affected by the electric field is negligibly small [11] compared to the surface area of the electrode, providing very little relaxation in the  $x$ -direction. The bottom surface was also fixed in a similar fashion to fix the stem into place, while the top surface was Nose-Hoover thermostat with a time constant of 0.1 ps was used to keep the temperature at 300 K during the course of the simulation and Nose-Hoover barostat with a time constant of 1 ps was used to keep the pressure in the  $z$ -direction  $p_{zz}$  at 0 Pa. The electric field was modeled as a vertical force in the  $y$ -direction acting on the surface atoms. The surface atoms were found dynamically during the course of the simulation by first excluding all atoms outside the geometric region where surface atoms could be found to reduce the computational load and secondly calculating the coordination number with a spherical cut-off value of 5 for the remaining atoms following the necessary condition described in Section 2.4.1. The coordination number under which an atom belongs to the surface was chosen to be 37. This number was chosen so that the surface would be covered to as great extent as possible while excluding bulk atoms with low coordination numbers, like atoms belonging to grain boundaries and the resulting surface is presented in Section 4.2. Whether an atom belongs to the surface and therefore is applied a force was re-assessed using coordination analysis every 10 timesteps (20 ps).

The magnitude of the additional force acting on each surface atom was calculated as:

$$f = \frac{pS_{\perp}}{N} = \frac{pLz}{N} \quad (3.3.1)$$

Where  $p$  is the exerted tensile stress on the system,  $L$  is the extent of atoms in the  $x$ -direction,  $z$  is the extent of atoms in the  $z$ -direction and  $N$  is the number of surface atoms. The exerted tensile stress  $p$  was increased slowly linearly in time to prevent the formation of pressure waves in the system [52] with a rate of  $\frac{dp}{dt} = Kp_0$  for 600 ps ( $3 \cdot 10^5$  timesteps), where  $K = 150 \frac{1}{\text{ps}}$  and  $p_0 = \frac{\epsilon_0 E_0^2}{2}$  is a reference stress corresponding to a reference electric field  $E_0 = 100 \frac{\text{MV}}{\text{m}}$ . The number of atoms  $N$  and the size of the system in the  $z$ -direction was monitored during the run and the forces were adjusted accordingly.

### 3.3.2 Spatially varying electric field

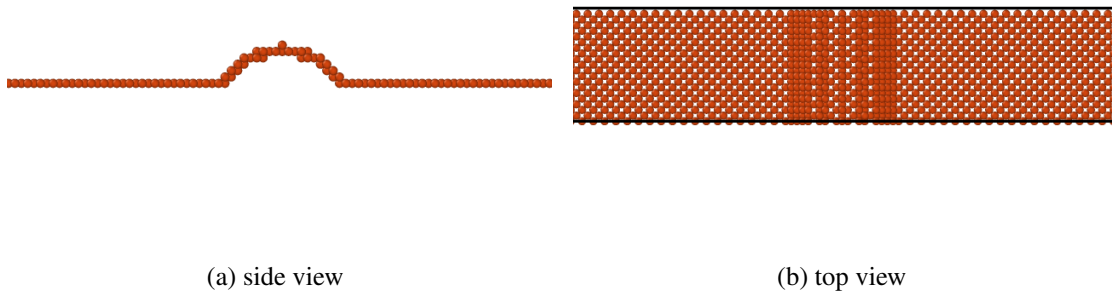
To apply a varying surface stress caused by varying electric field, the electric field distribution is calculated using Finite Element Method. The surface of the sample is found by similar means as described in the previous section. Custom-written Python scripts are used to create the number of points representing the surface with a spatial bin size of  $d = 1a = 3.6$ . The resulting points were imported into COMSOL and piece-wise cubic splines were used to interpolate a smooth surface between the points.

From this, the electric field distribution everywhere and in particular, on the surface was found and used to calculate the electrostatic stress distribution on the surface. This information, along with the surface normal vectors  $n_x, n_y$  at each point on the surface was exported to an external custom python script which divided the surface into spacial bins with bin size of  $\delta x = 0.5a = 1.875$ . In each bin, the stress acting on the surface element was averaged and the total force components  $\Delta F_x, \Delta F_y$  were calculated as described in Section 3.5. The force components were calculated for reference electric field of  $E_0 = 100 \frac{\text{MV}}{\text{m}}$ . The MD simulation was set up similarly as in the previous section to make comparison possible. System boundaries in the  $x$ -direction and on the bottom were fixed. Temperature was controlled with N-H thermostat and kept at 300 K. N-H barostat was used to keep  $p_{zz}$  at 0 Pa. The system was divided into  $\frac{L}{\delta x}$  bins and for each bin, the corresponding force components were read from the file and applied to the surface atoms after being normalized by the number of atoms in that particular bin. The atoms belonging to the surface were found dynamically every 10 timesteps and the forces on each atom was calculated. As in previous section, the forces on each surface element were ramped up linearly with time with a rate of  $\frac{d\vec{F}}{dt} = K\vec{F}_0$ , where  $\vec{F}_0$  corresponds to the force acting on a particular surface element in the case of applied reference electric field  $E_0$  and  $K = \frac{1}{150 \text{ ps}}$ . The directions of the forces on the surface element were not modified during the course of the run but only increased in magnitude. Also this approach does not take into account the changing electric field distribution due to the changing surface, but until major surface modification takes place, this approach remains valid. The simulation was run for 1000 ps.

## 4 Results and analysis

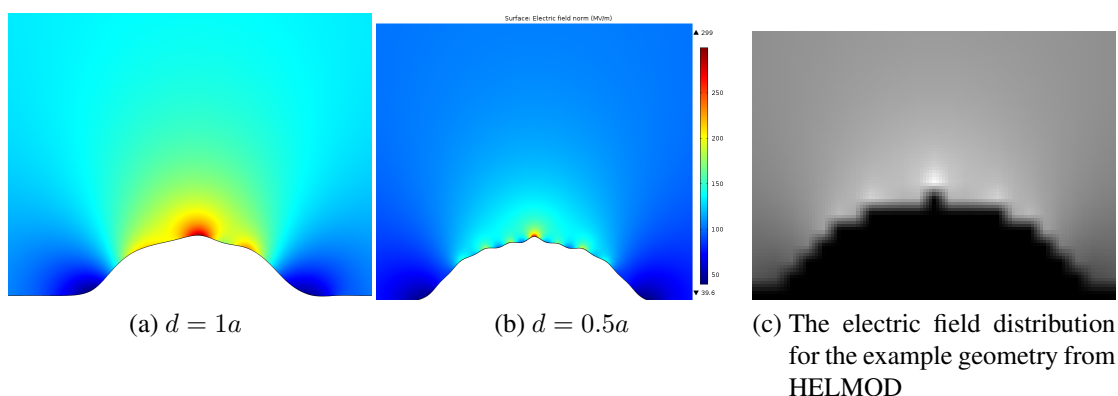
### 4.1 Surface reconstruction and electric field calculation for the test geometry

Figure 4.1.1: Atomistic surface of the test system



The atomic surface of the test geometry was obtained using the methods presented in Section 2.4.1 and is given in Figure 4.1.1. As can be seen, the surface is 1 atomic layer thick in flat regions and contains no holes, as is necessary. The electric field distributions corresponding to the surfaces created with different bin sizes as described in Section 3.1 are shown in Figure 4.1.2. The colors represent the electric field strength. The electric field is locally increased in the vicinity of the protrusion and tends to the reference electric field value further away from the protrusion. In the case of bin size  $d = 0.5a$ , where  $a = 3.615 \text{ \AA}$ , the lattice constant of copper, the maximum field enhancement is  $\beta = 3$  and in the case of bin size  $d = 1a$ , the field enhancement is around 1.6. It can be seen from the figures, that in the case of a bin size of  $1a = 3.615 \text{ \AA}$  the smoothed surface follows the initial atomistic surface more closely. For comparison, the electric field calculation conducted by Stefan Parviainen from University of Helsinki with HELMOD code is given in Figure 4.1.2 (c). His results show that the maximum field enhancement is around 1.8 which compares better with the case of bin size of  $1a$ , so this bin size is used for surface reconstruction of the polycrystal system under study.

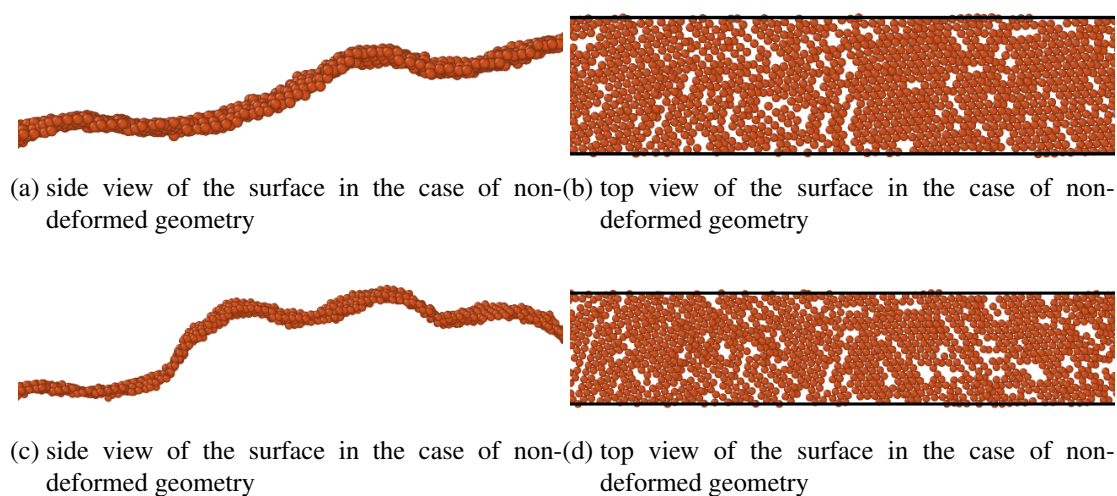
Figure 4.1.2: resulting FEM surfaces with the electric field distribution corresponding to different bin sizes



## 4.2 Surface reconstruction from molecular dynamics data for the system

Using the methods described in Section 2.4 surface reconstruction for the system was obtained. Two snapshots of the system at different times during the stress increase are given in Figure 4.2.1. The first figure shows the surface in the beginning of the simulation with no deformation present. It can be seen, that the necessary conditions for the surface detection algorithm are met - the surface is 1-2 lattice spacings thick and there very few holes in the surface. The second figure shows the surface in the course of the simulation, where there is noticeable surface deformation present. It can be seen that the quality of the surface is similar to the surface of the non-deformed geometry and so conforms to the criteria for the surface detection algorithm described in Section 2.4.1.

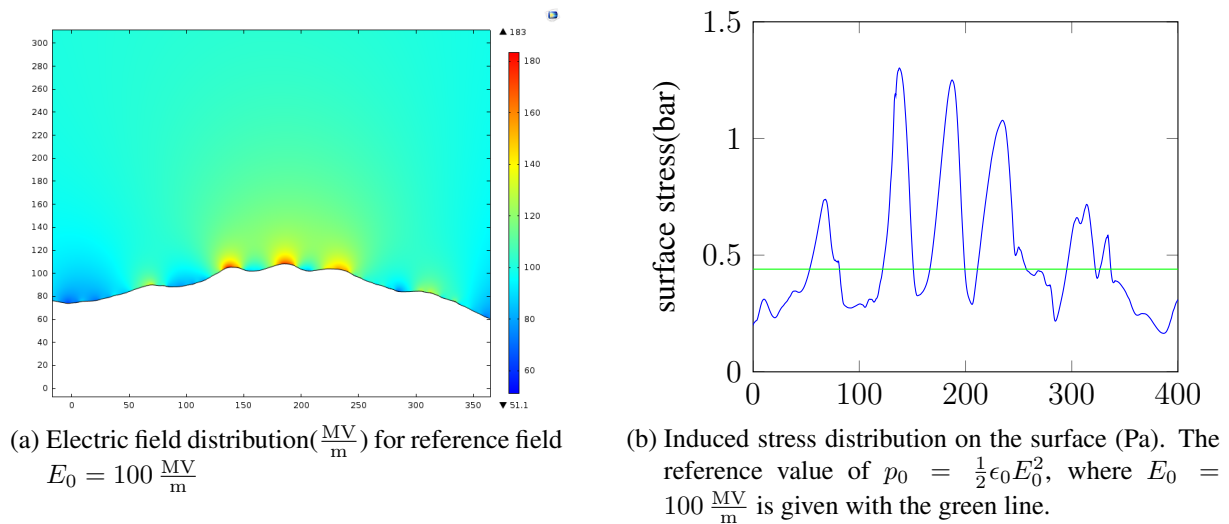
Figure 4.2.1: Surfaces found with coordination analysis



## 4.3 The electric field calculation with Finite Element Method

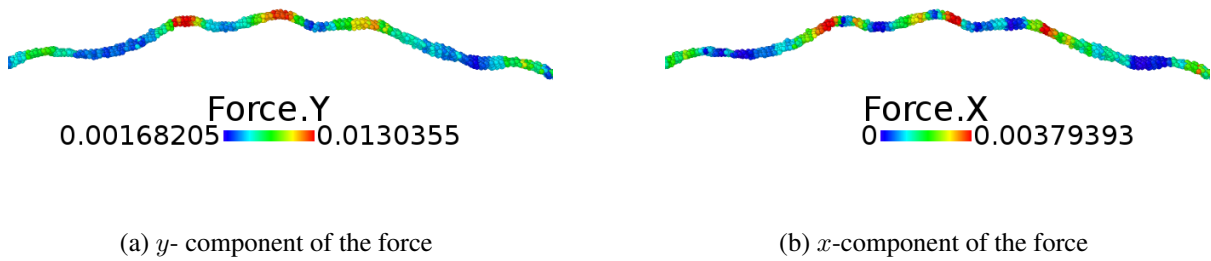
The electric field distribution calculated with methods described in Section 3.5.3 and the resulting induced electrostatic stress distribution on the surface is given in Figures 4.3.1a and 4.3.1b, respectively. For clarity, only the section of the surface with high surface roughness as compared to the rest of the sample is depicted. The colors represent the electric field strength above the material surface. It can be seen from the figure, that the greatest electric field enhancement is right above the places with greatest surface roughness as is expected. The electric field and the electric field-induced stress distributions are calculated for the reference electric field value of  $100 \frac{\text{MV}}{\text{m}}$ . Only part of the surface with greatest surface roughness is displayed for clarity. Greatest field enhancement  $\beta$  is around 1.8. As can be seen from Figure 4.3.1b, even a modest field enhancement can cause significantly varying induced stress distribution, with maximum enhancement by a factor of  $\beta^2 = 3.2$ , and maximum to minimum stress ratio being more than 5. The force components on each surface atom derived from the stress distribution as described

Figure 4.3.1: Electric field distribution



in Section 2.4.4 is shown in Figure 4.3.2. For clarity, only a section of the surface with greatest surface roughness is shown. This validates the method devised to apply electrostatic force on surface atoms used in present work and presented in Section 2.4. It can be seen from the figure, that the force distribution generally follows the stress distribution found in previous paragraph. The match is not exact as expected, as the total force acting on each surface element must be normalized with the number of atoms in that element, to obtain the forces on the surface atoms to ensure the total force acting on the surface atoms is equal to the force calculated from FEM calculations.

Figure 4.3.2: Electrostatic force on surface atoms



## 4.4 Results of preparing the sample

The internal structure of the system after each step of preparation is shown in Figure 4.4.1. The resulting internal crystal structure of the system was analyzed at each step of preparation. It is clearly visible that the number of defects has been reduced. A number of stacking faults have relaxed into the surrounding fcc structure. The grain boundaries have become more defined and the amorphous regions near the grain boundaries have disappeared. The initial surface roughness has decreased. To quantify the reduction of defects present in the sample, Common Neighbour Analysis was used to identify the atoms at each step of the preparation process and the number of each type of atoms was counted. It can be seen from Figure 4.4.2 that the overall number of atoms in their default fcc-like orientation has increased. After the first step, the amount of stacking faults increase, most probably due to dissociation of initially present dislocations into partial dislocations. It can be seen from the figure, that the decrease in the number of defects decreases with each successive step.

Figure 4.4.1: Steps for preparing the system. Green denotes fcc atoms, red - hcp, grey- amorphous(undefiend)

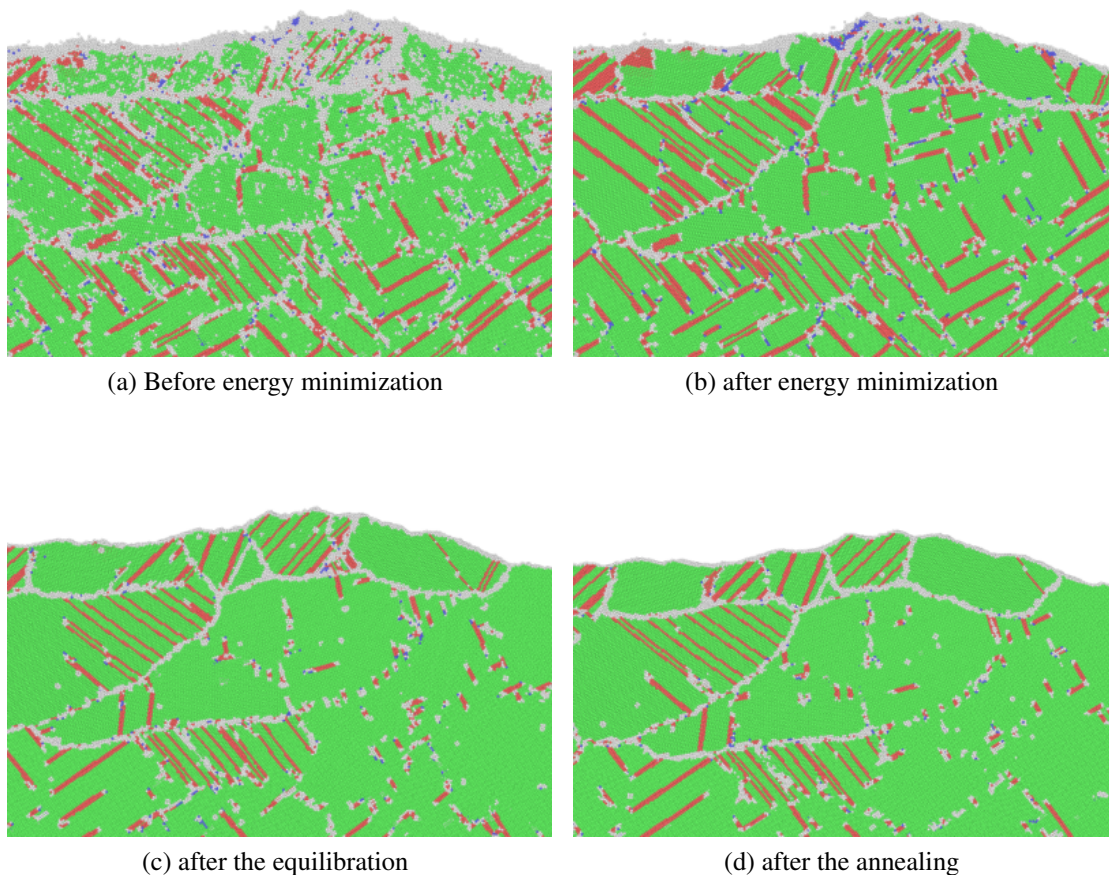
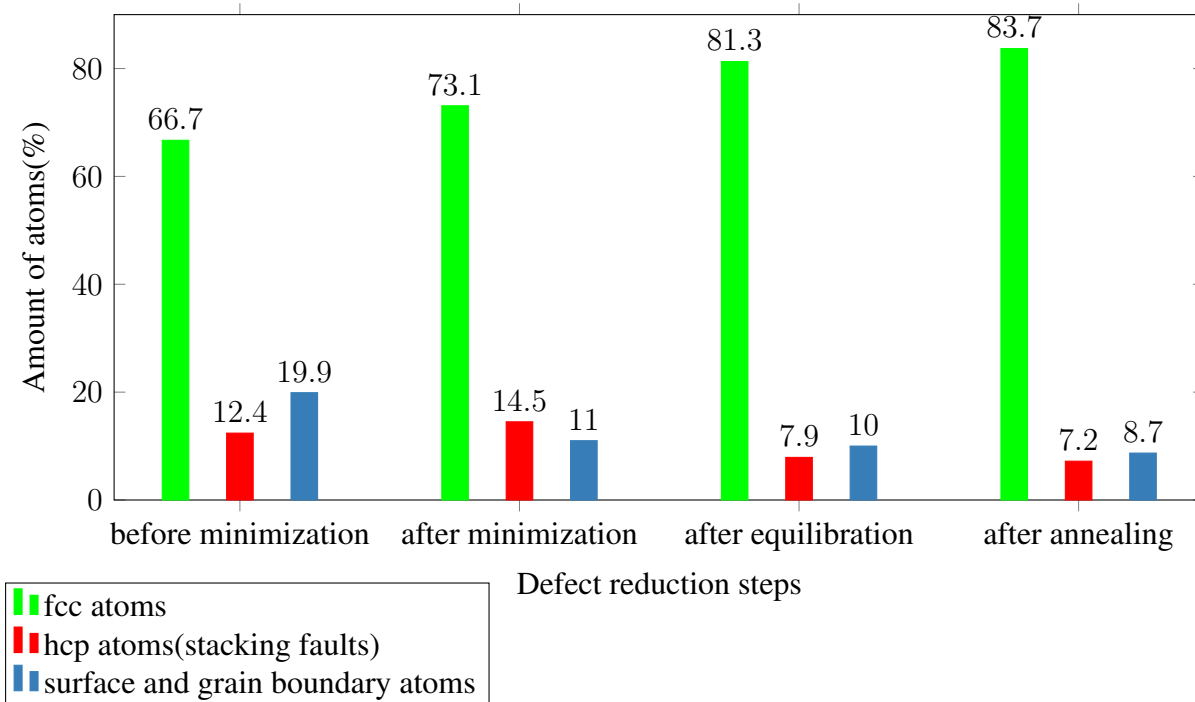
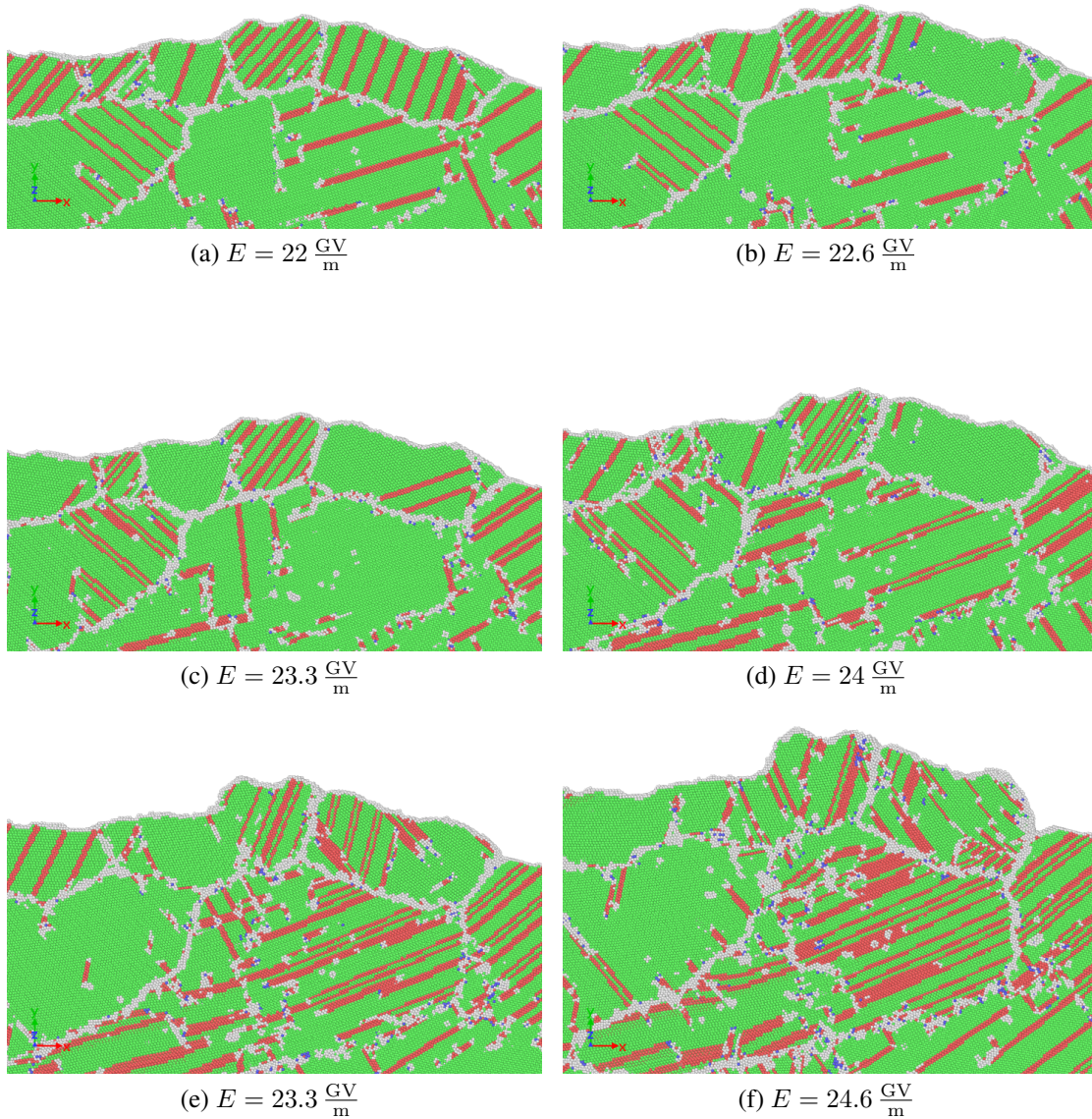


Figure 4.4.2: Atom types in the sample



## 4.5 MD Simulation results of material under constant surface electric field

Figure 4.5.1: Deformation steps with constant stress



The resulting snapshots of the simulation with constant surface electric field as described in Section 3.3.1 is given in Figure 4.5.1 and the internal crystal structure during the deformation is found using common neighbour analysis. As the electric field and thereby the surface stress is increased, the creation of additional structure defects and in particular a large number of stacking faults can be observed. Massive surface modification starts around the electric field value of  $24.6 \frac{\text{MV}}{\text{m}}$ . The surface exhibits sharp breaking points near the places the grain boundary intersects with the surface.

## 4.6 MD simulation results of material under spatially varying surface electric field

Figure 4.6.1: Deformation steps with spatially varying electric field. Atoms are color-coded with CNA.

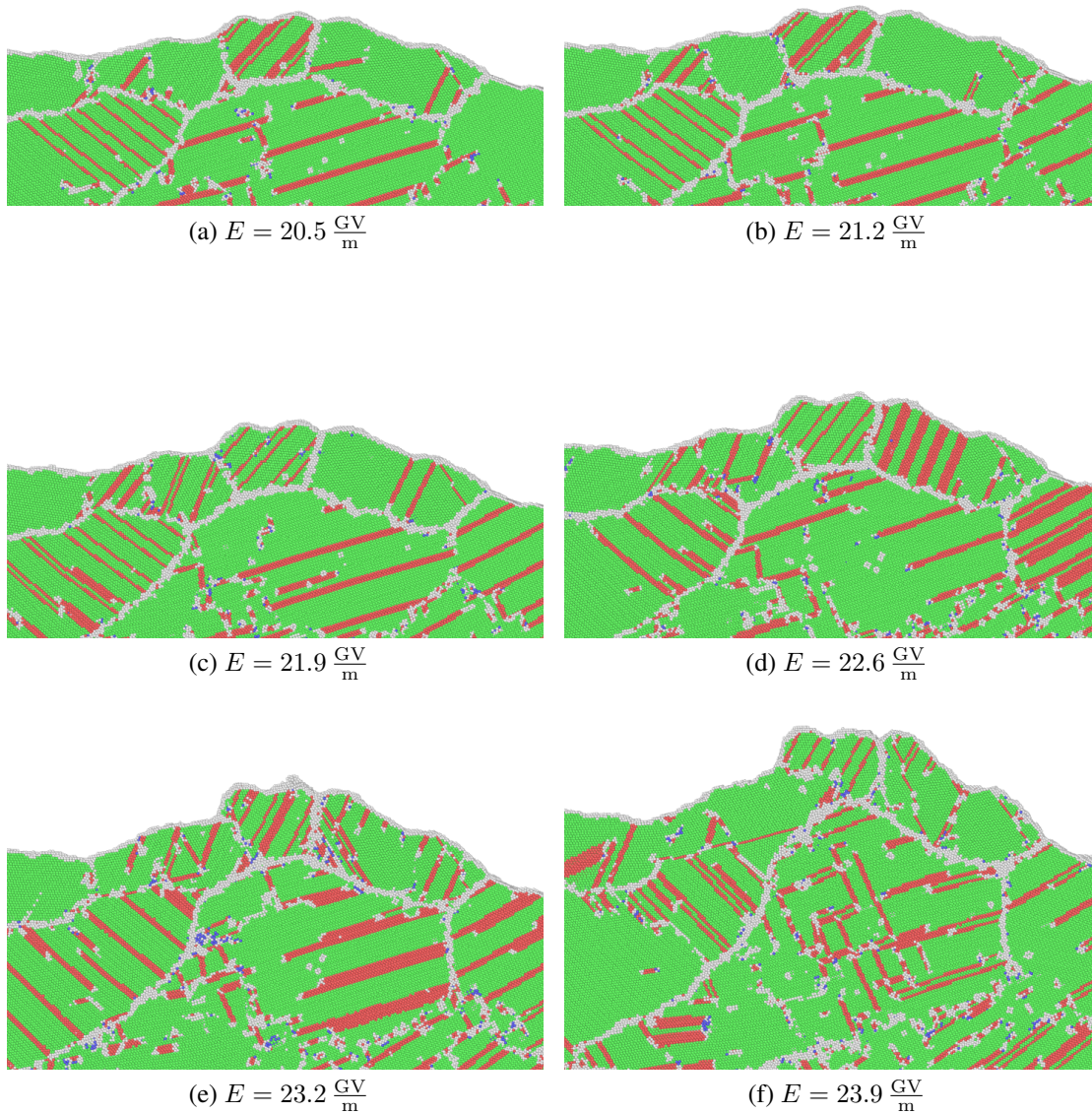
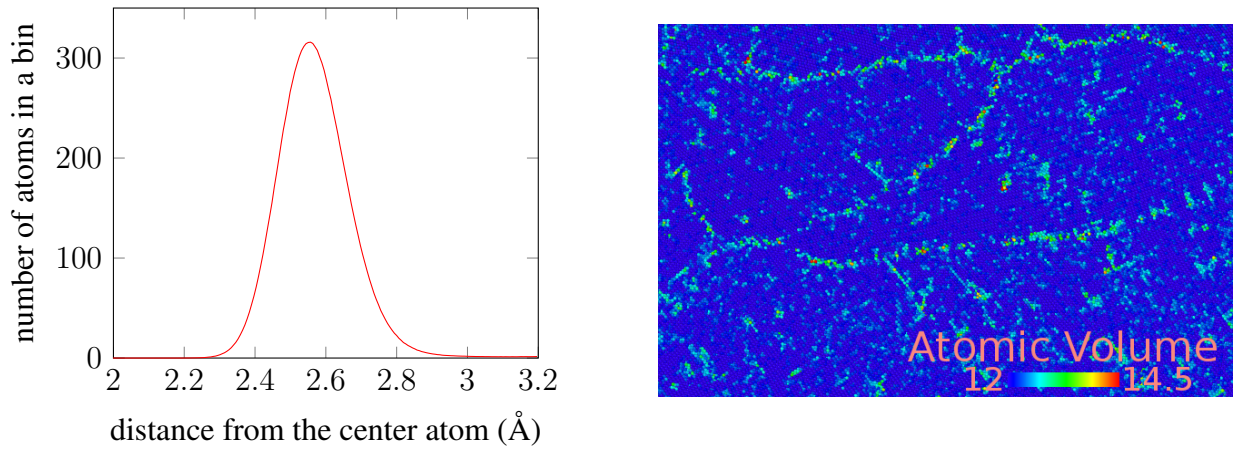


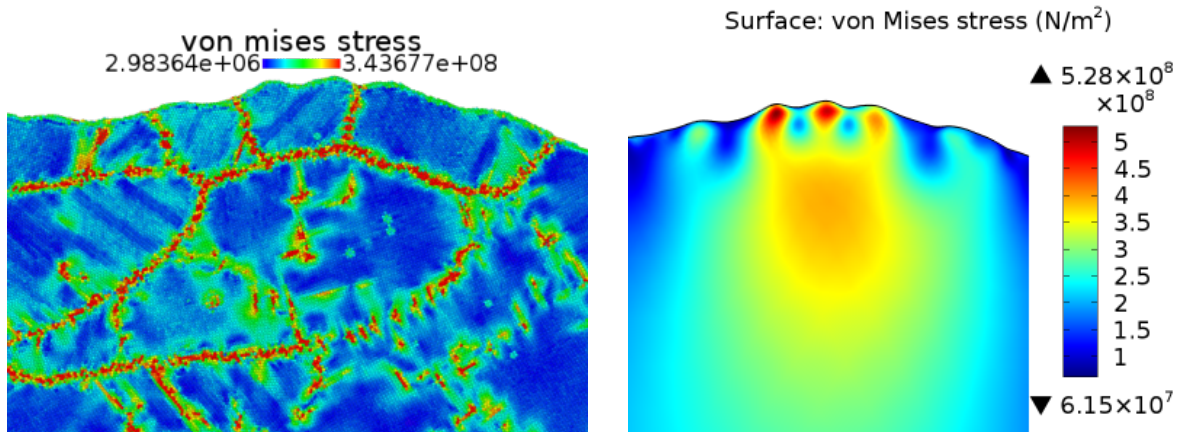
Figure 4.6.2: Voronoi analysis and the radial distribution function



(a) Radial distribution function of the system. The cut-off value is chosen to be 3.2

(b) voronoi volumes

Figure 4.6.3: Stress distribution, varying electric field,  $E_0 = 10 \frac{\text{GV}}{\text{m}}$



(a) Von mises stress from LAMMPS (Pa)

(b) Von mises stress from Comsol (Pa)

The resulting snapshots of the simulation with spatially varying electric field is displayed in Figure 4.6.1. Significant surface modification starts around electric field value of  $E = 21.5 \frac{\text{GV}}{\text{m}}$ . As expected, this value is lower than the critical electric field value for the case of constant surface electric field described in the last section, which does not take the electric field enhancement into account. During the ramping of the electric field, creation of additional stacking faults can first be observed which are annihilated when large-scale plastic deformation occurs and dislocations reach the surface, restoring the local fcc crystal configuration within grains. The places where the grain boundaries intersect with the surface provide a natural starting point for the onset of surface deformation, with the side subject to a greater induced stress bending the grain boundary causing the underlying grains to deform. To study the onset of plastic deformation in the system, Von Mises stress distribution in the material was calculated with finite element method (Figure 4.6.2a) and molecular dynamics (Figure 4.6.2b) for the electric field value of

$E_{stress} = 10 \frac{GV}{m}$ . The mean atomic volume of the atoms in the system necessary to calculate the atomic stress tensor components in MD was found by calculating the radial distribution function for the system at that electric field value. The mean atomic volume is taken to be  $\frac{4}{3}\pi r_{mean}^3 = 8.74 \text{ \AA}^3$ , where  $2r_{mean} = 2.56 \text{ \AA}$  is the value corresponding to the maximum of the radial distribution function, which is given in Figure 4.6.3a. For comparison, the atomic volumes of atoms calculated by Voronoi tessellation of a representative part of the system and are shown in Figure 4.6.3b. It can be seen, that the atomic volumes differ by less than 20% which justifies the calculation of atomic stress using the mean volume of the atoms, as the atomic *stress · volume* in the atomic system can differ up to two orders of magnitude. As expected in the FEM calculation which assumes an isotropic material structure, the electric field-induced surface stress creates a smoothly varying stress field decaying with distance from the surface. In the MD case, the long range decaying stress field cannot be directly seen and instead stress is concentrated in the grain boundaries, where the stress can be up to two orders of magnitude larger than in the bulk of the grains. A particular feature of the stress field acquired with FEM is the creation of a region with increased stress below the three small regions of greatest surface roughness, which extends far beyond the characteristic length scale of the protrusions and reaches a maximum at some distance in the material. In the MD picture, this regions corresponds to a grain boundary parallel to the surface which does not let the stress to penetrate into the grain below. It can be seen

## 4.7 Discussion

As expected, the simulation which takes inherent surface roughness into account exhibits a lower critical electric field value for surface deformation than the simulation which does not. The magnitudes of the electric field used both in current work and in previous studies [14][12] are high as compared to the conditions present in the accelerating structures of CLIC to allow for plastic deformation to take place in the time frames achievable by molecular dynamics simulations. This can also be partially explained by the fact, that experimentally the local field enhancement factor on copper surfaces has never been observed to be less than 10[7] present in the accelerating structures of CLIC to allow for plastic deformation to take place in the time frames achievable by molecular dynamics simulations.. The critical electric field values found in current work are somewhat higher than than the onset electric field value for catastrophic failure for the case of a nanovoid under the surface as found in [10] but the approach followed there takes into account the electric field distribution change with the surface modification. If this is not taken into account as in [11] and [14], the onset electric field for massive surface modification is comparable to the results of present work. The critical field values acquired are below the experimental value for the field evaporation of pure copper, which is around  $30 \frac{GV}{m}$  [53, 47]. This indicates that the the material defects in models simulated in present work reduce the necessary electric field strength for field evaporation and thereby for plasma formation, as an increasing surface roughness increases the electric field which leads to a self-reinforcing process because of which, the critical field strength needed for field evaporation is not appreciatively larger than the field needed for massive surface deformation [10]. The processes of field evaporation and plasma formation themselves are not discussed in present work, as those processes lie outside the scope of validity of used methods. The crucial step in the developed methods is obtaining a smooth surface necessary for continuum calculations from atomistic data. Although the method developed in current work performs well for the problem under study with modest surface roughness concerning the electric field- induced surface stress,

further study is needed to obtain detailed parametrization of the electric field distribution near an atomistic rough surface, to study strong field-dependant effects like electron field emission, which is very sensitive to the local electric field.

## Summary

The electrical breakdown phenomenon in particle accelerators, fusion reactors and other high energy structures is of continuing practical and theoretical interest, as many processes concerning the nature of those breakdowns remains unclear. It is believed that in many cases the breakdown event might be initiated by the surface deformation due to material failure in strong electric fields, which is governed by the intrinsic defects in the material. In current work a computer model of nano-crystalline copper was prepared to study the surface modification due material defects in a system under the influence of strong electric fields. For that effect, classical molecular dynamics was used along with methodology developed and validated in current work to use the atomic data for continuum electric field calculation with finite element method. This was conducted to take into account the inherent surface roughness of the system under study.

To prepare the system for further simulations, the number of defects initially present in the material was reduced using energy minimization and simulated annealing. To take into account the electric field distribution and the resulting stress distribution on the material surface, methods were developed and implemented to move between the atomistic representation of the system simulated with molecular dynamics and the continuum representation of the system simulated with finite element method. The critical electric field values for massive surface deformation in the case of constant surface electric field and spatially varying electric were found to be  $24.6 \frac{\text{GV}}{\text{m}}$  and  $21.5 \frac{\text{GV}}{\text{m}}$ , respectively, the lower of which is similar to the values found in various other simulations of copper defects [11][14]. For comparison, the stress distribution in the material was calculated with FEM and MD. The failure mechanisms of the underlying grain structure and the resultant surface deformation was analyzed. The electric field-induced surface stress created large-scale deformation of the grains underlying the regions with greatest electric field value. The methods described here to calculate the electric field distribution from atomistic data work sufficiently well for the system currently under study, but further refinement is needed to capture strongly field-dependant effects.

# Kokkuvõte

## Nanokristalse vase simulatsioonid tugevates elektriväljades

Elektrilised läbilöögid kõrgetel pingetel töötavatel seadmetes pakuvad teadlastele jätkuvalt huvi nii praktilisest kui teoreetilisest vaatepunktist, kuna paljuski on nende läbilöökid tekkepõhjused teadmata. Üks võimalikke seletusi on, et elektrilisi läbilööke neis struktuurides põhjustab materjali pinna deformatsioon tugevate elektriväljade mõjul, materjali pinna vahetus läheduses paiknevate materjalidefektide tõttu. Käesolevas töös valmistati ette nano-kristalse vase polükristalli arvutimudel, et uurida selle pinna võimalikku modifikatsiooni tugevates elektriväljades materjalidefektide tõttu. Simulatsioonimeetodina kasutati süsteemi atomistlikuks esitamiseks klassikalist molekulaardünaamikat ning pideva keskkonna mudelina lõplike elementide meetodit. Nende kahe lähenemise ühendamiseks vaja minev metoodika ning implentatsioon töötati välja käesolevas töös.

Järgnevate simulatsioonide ette valmistamiseks oli vaja süsteemis sisalduvate materjalidefektide arvu vähendada ning seda tehti kasutades energia minimeerimist ning simuleeritud lõõmutamist. Välja töötatud elektrivälja arvutamise mudelit kasutati uurimaks tugevate elektriväljade mõju materjali pinnale. Viidi läbi simulatsioonid konstantse elektriväljaga ning materjali pinna geomeetriast sõltuva elektriväljaga. Elektrivälja väärtused, kus hakkas pihta tugev pinna deformatsioon leiti olevat vastavalt  $24.6 \frac{GV}{m}$  ning  $21.5 \frac{GV}{m}$ . Pinna geomeetriast sõltuva väljaga simulatsiooni korral oli kriitiline elektrivälja tugevus sarnane eelnevate töödega [11] [14]. Mehaanilise pinge jaotused materjalis leiti nii molekulaardünaamikast kui lõplike elementide meetodit kasutades, et uurida materjali sisemuses toimuva deformatsiooni olemust. Tugevaima elektriväljaga pinna osa all tekitas pinnale mõjuv elektrivälja tugeva mehaanilise pinge regiooni, mistõttu seal asuv kristalliidi sein deformeerus märgatavalt. Siinkirjeldatud elektrivälja arvutamise algoritm näitas käesoleva probleemi lahendamiseks head töökindlust, kuid edasist uurimist on vaja, et saavutada piisavalt hea täpsus, et simuleerida ka elektri väljast tugevamini sõltuvaid efekte.

## Acknowledgements

I would like to thank my supervisors Vahur Zadin and Flyura Djurabekova for their guidance, example and support in writing this theses. Second I would like to thank the people of Accelerator Lab at the Department of Physics at the University of Helsinki for the inspiration and ideas for the current work. Third I would like to thank my fellow students Kristjan Eimre and Simon Vigonski for fruitful academic discussions. Special thanks goes to Ants Remm and Madis Ollikainen for their companionship and endless inspiring discussion about physics during the past years. Last but not least I want to thank my friends and family for their endless support. Without them this thesis would not have been completed.

# Bibliography

- [1] How Supercomputers Will Yield a Golden Age of Materials Science - Scientific American.
- [2] Ellad B. Tadmor. *Modeling materials: continuum, atomistic, and multiscale techniques*. Cambridge University Press, Cambridge ; New York, 2011.
- [3] N. Holtkamp. The status of the ITER design. *Fusion Engineering and Design*, 84(2–6):98–105, June 2009.
- [4] W. Wuensch. Observations about RF Breakdown from the CLIC High Gradient Testing Program. 2006.
- [5] M Aicheler and European Organization for Nuclear Research. *A Multi-TeV linear collider based on CLIC technology: CLIC Conceptual Design Report*. CERN, Geneva, 2012.
- [6] H. Braun, S. Döbert, I. Wilson, and W. Wuensch. Frequency and Temperature Dependence of Electrical Breakdown at 21, 30, and 39 GHz. *Physical Review Letters*, 90(22), June 2003.
- [7] A. Descoedres, Y. Levinsen, S. Calatroni, M. Taborelli, and W. Wuensch. Investigation of the dc vacuum breakdown mechanism. *Physical Review Special Topics - Accelerators and Beams*, 12(9):092001, September 2009.
- [8] A. Descoedres, T. Ramsvik, S. Calatroni, M. Taborelli, and W. Wuensch. dc breakdown conditioning and breakdown rate of metals and metallic alloys under ultrahigh vacuum. *Physical Review Special Topics - Accelerators and Beams*, 12(3):032001, March 2009.
- [9] S. Parviainen, F. Djurabekova, H. Timko, and K. Nordlund. Electronic processes in molecular dynamics simulations of nanoscale metal tips under electric fields. *Computational Materials Science*, 50(7):2075–2079, May 2011.
- [10] A. S. Pohjonen, S. Parviainen, T. Muranaka, and F. Djurabekova. Dislocation nucleation on a near surface void leading to surface protrusion growth under an external electric field. *Journal of Applied Physics*, 114(3):033519, July 2013.
- [11] A. S. Pohjonen, F. Djurabekova, K. Nordlund, A. Kuronen, and S. P. Fitzgerald. Dislocation nucleation from near surface void under static tensile stress in Cu. *Journal of Applied Physics*, 110(2):023509, July 2011.
- [12] Flyura Djurabekova Simon Vigonski. Molecular dynamics simulations of near-surface Fe precipitates in Cu under high electric fields. *Modelling and Simulation in Materials Science and Engineering*, 23(2), 2015.

- [13] Rod V. Latham, editor. *High voltage vacuum insulation: basic concepts and technological practice*. Acad. Press, London, 1995.
- [14] S. Parviainen, F. Djurabekova, A. Pohjonen, and K. Nordlund. Molecular dynamics simulations of nanoscale metal tips under electric fields. *Nuclear Instruments and Methods in Physics Research Section B: Beam Interactions with Materials and Atoms*, 269(14):1748–1751, July 2011.
- [15] Derek Hull and D. J. Bacon. *Introduction to dislocations*. Butterworth-Heinemann, Oxford [Oxfordshire] ; Boston, 4th ed edition, 2001.
- [16] Daniel Mayer and DrBob. "Cubic-face-centered" by Original PNGs by Daniel Mayer and DrBob, traced in Inkscape by User:Stannered - Cubic, face-centered.png Lattice face centered cubic.svg. Licensed under CC BY-SA 3.0 via Wikimedia Commons - <http://commons.wikimedia.org/wiki/File:Cubic-face-centered.svg#/media/File:Cubic-face-centered.svg>.
- [17] Daniel Mayer and DrBob. "Cubic-body-centered" by Original PNGs by Daniel Mayer, DrBob, traced in Inkscape by User:Stannered - Crystal structure. Licensed under CC BY-SA 3.0 via Wikimedia Commons - <http://commons.wikimedia.org/wiki/File:Cubic-body-centered.svg#/media/File:Cubic-body-centered.svg>.
- [18] Mohammed Cherkaoui and Laurent Capolungo. *Atomistic and Continuum Modeling of Nanocrystalline Materials*, volume 112 of *Springer Series in Materials Science*. Springer US, Boston, MA, 2009.
- [19] B. J. Alder and T. E. Wainwright. Studies in Molecular Dynamics. I. General Method. *Journal of Chemical Physics*, 31:459–466, August 1959.
- [20] D. C. Rapaport. *The art of molecular dynamics simulation*. Cambridge University Press, Cambridge, UK ; New York, NY, 2nd ed edition, 2004.
- [21] Shuichi Nosé. A unified formulation of the constant temperature molecular dynamics methods. *The Journal of Chemical Physics*, 81(1):511–519, July 1984.
- [22] William G. Hoover. Canonical dynamics: Equilibrium phase-space distributions. *Physical Review A*, 31(3):1695–1697, March 1985.
- [23] Peter Young. The leapfrog method and other “symplectic” algorithms for integrating Newton’s laws of motion - <http://young.physics.ucsc.edu/115/leapfrog.pdf>.
- [24] William H. Press, editor. *Numerical recipes: the art of scientific computing*. Cambridge University Press, Cambridge, UK ; New York, 3rd ed edition, 2007.
- [25] Loup Verlet. Computer "Experiments" on Classical Fluids. I. Thermodynamical Properties of Lennard-Jones Molecules. *Physical Review*, 159(1):98–103, July 1967.
- [26] Murray S. Daw and M. I. Baskes. Embedded-atom method: Derivation and application to impurities, surfaces, and other defects in metals. *Physical Review B*, 29(12):6443–6453, June 1984.

- [27] Murray S. Daw, Stephen M. Foiles, and Michael I. Baskes. The embedded-atom method: a review of theory and applications. *Materials Science Reports*, 9(7–8):251–310, March 1993.
- [28] Y. Mishin, M. J. Mehl, D. A. Papaconstantopoulos, A. F. Voter, and J. D. Kress. Structural stability and lattice defects in copper: Ab initio, tight-binding, and embedded-atom calculations. *Physical Review B*, 63(22):224106, May 2001.
- [29] Q. X. Pei, C. Lu, F. Z. Fang, and H. Wu. Nanometric cutting of copper: A molecular dynamics study. *Computational Materials Science*, 37(4):434–441, October 2006.
- [30] Hongwu Zhang, Yifei Fu, Yonggang Zheng, and Hongfei Ye. Molecular dynamics investigation of plastic deformation mechanism in bulk nanotwinned copper with embedded cracks. *Physics Letters A*, 378(9):736–740, February 2014.
- [31] Christian Brandl, Timothy C. Germann, Alejandro G. Perez-Bergquist, and Ellen K. Cerreta. Grain Boundary Motion under Dynamic Loading: Mechanism and Large-Scale Molecular Dynamics Simulations. *Materials Research Letters*, 1(4):220–227, December 2013.
- [32] 4.2. Atomic stress tensor analysis — CURP document 1.0 documentation.
- [33] Xinming Qiu Bin Liu. How to Compute the Atomic Stress Objectively? *Journal of Computational and Theoretical Nanoscience*, 6(5), 2008.
- [34] [http://lammps.sandia.gov/doc/compute\\_stress\\_atom.html](http://lammps.sandia.gov/doc/compute_stress_atom.html). lammps manual.
- [35] Allan F. Bower. *Applied mechanics of solids*. CRC Press, Boca Raton, 2010.
- [36] S. M. A Kazimi. *Solid mechanics*. Tata McGraw-Hill, New Delhi, 1984.
- [37] Rodney Hill. *The mathematical theory of plasticity*. Number 11 in Oxford engineering science series. Clarendon Press ; Oxford University Press, Oxford : New York, 1998.
- [38] Daan Frenkel and Berend Smit. *Understanding molecular simulation: from algorithms to applications*. Number 1 in Computational science series. Academic Press, San Diego, 2nd ed edition, 2002.
- [39] S. Kirkpatrick, C. D. Gelatt, and M. P. Vecchi. Optimization by Simulated Annealing. *Science*, 220(4598):671–680, May 1983.
- [40] Alexander Stukowski. Structure identification methods for atomistic simulations of crystalline materials. *Modelling and Simulation in Materials Science and Engineering*, 20(4):045021, June 2012.
- [41] J. Dana. Honeycutt and Hans C. Andersen. Molecular dynamics study of melting and freezing of small Lennard-Jones clusters. *The Journal of Physical Chemistry*, 91(19):4950–4963, September 1987.
- [42] Daniel Faken and Hannes Jónsson. Systematic analysis of local atomic structure combined with 3d computer graphics. *Computational Materials Science*, 2(2):279–286, March 1994.

- [43] Steve Plimpton. Fast Parallel Algorithms for Short-Range Molecular Dynamics. *Journal of Computational Physics*, 117(1):1–19, March 1995.
- [44] <http://lammps.sandia.gov/>. LAMMPS.
- [45] Alexander Stukowski. Visualization and analysis of atomistic simulation data with OVITO—the Open Visualization Tool. *Modelling and Simulation in Materials Science and Engineering*, 18(1):015012, January 2010.
- [46] John David Jackson. *Classical electrodynamics*. Wiley, New York, 3rd ed edition, 1999.
- [47] Adam Kiejna and Kazimierz F. Wojciechowski. *Metal surface electron physics*. Pergamon, Oxford, 1. ed edition, 1996.
- [48] Lin Lin Jensen and Lasse Jensen. Electrostatic Interaction Model for the Calculation of the Polarizability of Large Noble Metal Nanoclusters. *The Journal of Physical Chemistry C*, 112(40):15697–15703, October 2008.
- [49] Xue Ben and Harold S. Park. Atomistic simulations of electric field effects on the Young’s modulus of metal nanowires. *Nanotechnology*, 25(45):455704, November 2014.
- [50] Ossi Saresoja, Antti Kuronen, and Kai Nordlund. Atomistic Simulation of the Explosion Welding Process. *Advanced Engineering Materials*, 14(4):265–268, April 2012.
- [51] E. Polak. *Optimization: algorithms and consistent approximations*. Number 124 in Applied mathematical sciences. Springer-Verlag, New York, 1997.
- [52] David Cereceda, J. Manuel Perlado, and Jaime Marian. Techniques to accelerate convergence of stress-controlled molecular dynamics simulations of dislocation motion. *Computational Materials Science*, 62:272–275, September 2012.
- [53] J. H. Norem Z. Insepov. New mechanism of cluster field evaporation in rf breakdown. *Physical Review Special Topics-accelerators and Beams - PHYS REV SPEC TOP-AC*, 7(12):180– 181, 2004.

## **Non-exclusive licence to reproduce thesis and make thesis public**

I, Kristian Kuppert,

1. herewith grant the University of Tartu a free permit (non-exclusive licence) to:
  - 1.1. reproduce, for the purpose of preservation and making available to the public, including for addition to the DSpace digital archives until expiry of the term of validity of the copyright, and
  - 1.2. make available to the public via the university's web environment, including via the DSpace digital archives, as of **28.05.2018** until expiry of the term of validity of the copyright, (date)

Nanocrystalline copper simulations in high electric fields ,  
(title of thesis)

supervised by Vahur Zadin and Flyura Djurabekova,  
(supervisor's name)

2. I am aware of the fact that the author retains these rights.
3. This is to certify that granting the non-exclusive licence does not infringe the intellectual property rights or rights arising from the Personal Data Protection Act.

Tartu, **28.05.2015**